

# Analogue modelling of basin inversion: the role of oblique kinematics and implications for the Araripe Basin (Brazil)

Pâmela C. Richetti<sup>1,2</sup>, Frank Zwaan<sup>2,3,4</sup>, Guido Schreurs<sup>2</sup>, Renata S. Schmitt<sup>1,2,5</sup>, Timothy C. Schmid<sup>2</sup>

5 <sup>1</sup> Universidade Federal do Rio de Janeiro, Programa de Pós-graduação em Geologia-PPGL, Brazil

<sup>2</sup> University of Bern, Institute of Geological Sciences, Bern, Switzerland

<sup>3</sup> Helmholtz Centre Potsdam - GFZ German Research Centre for Geosciences, Potsdam, Germany

<sup>4</sup> University of Fribourg, Department of Geosciences, Fribourg, Switzerland

<sup>5</sup> Universidade Federal do Rio de Janeiro, Departamento de Geologia-IGEO, Brazil

10 Correspondence: Pâmela C. Richetti (pamelarichetti@geologia.ufrj.br)

## Abstract.

Basin inversion is a process that takes place when a sedimentary basin is subjected to compressional stresses resulting in the reactivation of pre-existing faults and/or localization of deformation along new reverse faults. The Araripe Basin (NE Brazil) is an example of a Cretaceous intracontinental aborted rift with its sedimentary infill found at ca. 1000 m altitude, ~~500 m above the host basement~~. Post-rift basin inversion has been proposed by previous authors as the cause of this topographic high, but how inversion affected this basin remains a matter of debate, with two end member scenarios: reactivation of pre-existing normal faults leading to local uplift, or regional uplift ~~and differential erosion~~. Neither end member fully explains the observations from seismic and field data. In this study, we, therefore, conducted analogue models to explore how basin inversion in the Araripe Basin could have taken place. We present two series of crustal-scale brittle-viscous experiments: i) extension followed by compression without sedimentation, with a variation in divergence and convergence directions (orthogonal or 45° oblique), and ii) extension ~~with syn-rift sedimentation~~ followed by compression ~~with syn-rift sedimentation~~, with the same variation in rifting and inversion directions. ~~We applied a seed representing a structural weakness at the base of the brittle layer to localize deformation along the model axis.~~ We found that orthogonal rifting without sedimentation forms through-going graben boundary faults, whereas oblique rifting initially creates *en échelon* faults that eventually link up creating large graben boundary faults. Rift basins with syn-rift sedimentation evolved in a similar fashion, however, sedimentary loading resulted in increased subsidence. During both oblique and orthogonal inversion, most shortening ~~is was~~ accommodated along new low-angle reverse faults. Significant intra-graben fault reactivation occurred in all models without syn-rift sedimentation. By contrast, orthogonal inversion of models with syn-rift sedimentation did not reactivate rift faults, whereas only minor reactivation of rift faults took place during oblique inversion since the sediments ~~acted as a buffer during convergence~~ ~~strengthened the otherwise weakened basin, thus acting as a buffer during convergence~~. Based on our modelling results, we propose an alternative scenario for the evolution of the Araripe Basin, involving oblique inversion and the development of low-angle reverse faults, which better fits observations from seismic lines and field data from the region.

## 1 Introduction

The inversion of sedimentary basins as a result of compressional tectonics is a widely discussed topic due to its importance for the development of mineral (Sibson and Scott, 1998) and hydrocarbon deposits (Turner and Williams, 2004). Especially inverted intraplate rift basins that are currently exposed above sea level can play an important role for the understanding of their offshore equivalents, since they provide access to outcrops that otherwise can only be analyzed via indirect geophysical methods (e.g., Stanton et al., 2014; Rebelo et al., 2021).

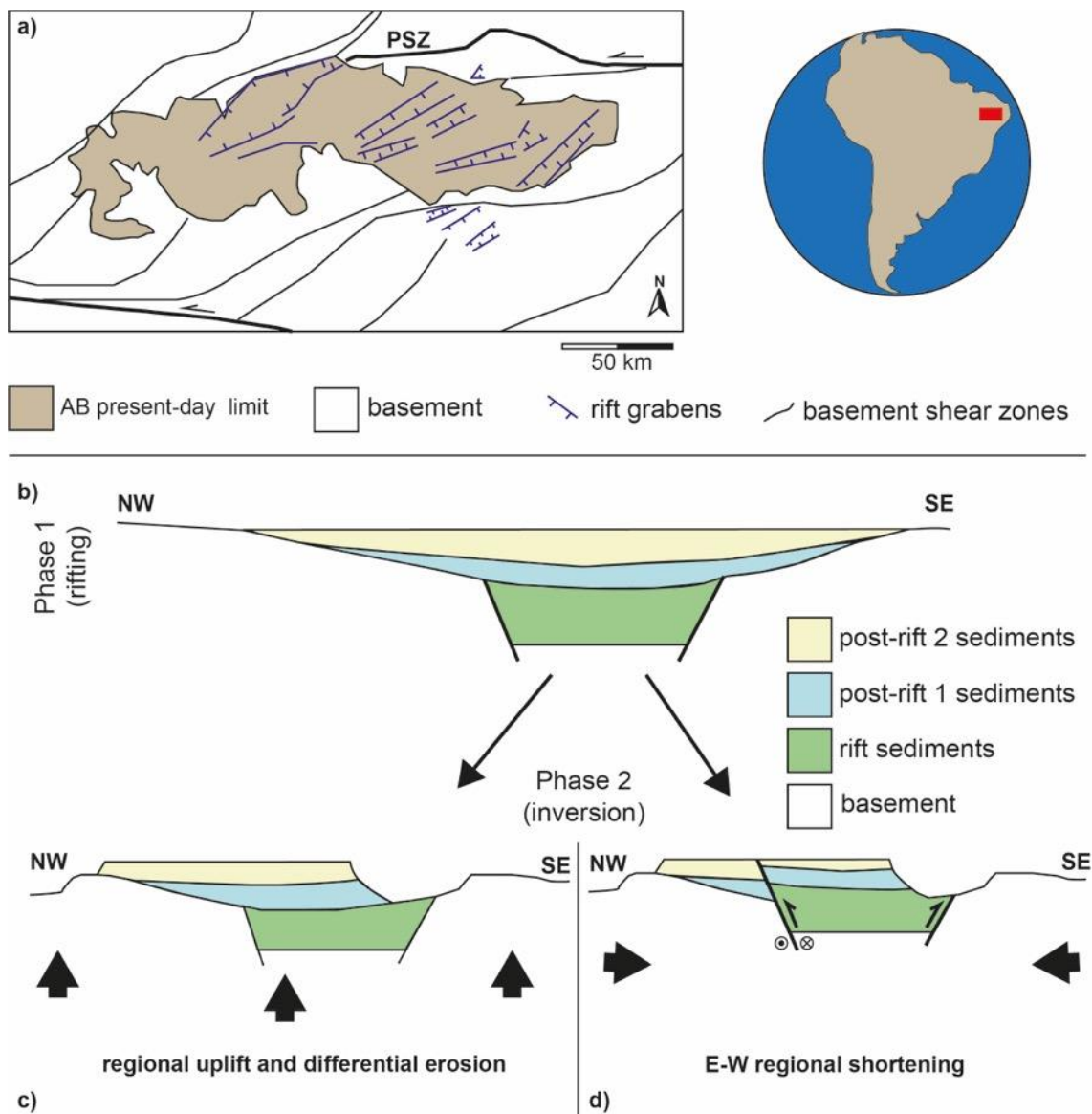
In this context, the Araripe Basin in NE Brazil is an excellent example of an exposed inverted intraplate rift basin (Fig. 1). This Early Cretaceous rift basin is part of the aborted Brazilian Northeast Rift System (BNRS) (de Matos, 1992) located at the intersection of the equatorial and central segments of the South Atlantic Ocean (Moulin et al., 2010). This rift system formed within the well-developed network of NE-SW and E-W striking Precambrian ductile shear zones in the basement of the Borborema Province (Fig. 1a) (Vauchez et al., 1995; Brito Neves et al., 2000; Ganade de Araujo et al., 2014). The rift structures within the E-W oriented Araripe Basin mainly strike NE-SW (Fig. 1a), indicating brittle reactivation of the basement shear zones during rifting (de Matos, 1992) (Fig. 1a). However, the exact kinematics of rifting during Araripe Basin formation remains a matter of debate, with some authors proposing orthogonal kinematics, whereas others invoke transtension (e.g., Rosa et al. 2023).

After rifting and subsequent thermal subsidence (Assine, 2007), the basin registered a phase of inversion (Fig. 1b) (Marques et al., 2014) and its sedimentary infill is presently situated, at its highest point, at 1000 m above sea level and ca. 500 m above the surrounding basement. Similarly, the Borborema Province generally contains high topographies and evidence of recent uplift (Lamarque and Julià, 2019; Neto et al., 2019), and other basins in the BNRS also present evidence of tectonic inversion (Gurgel et al., 2013; Nogueira et al., 2015; Vasconcelos et al., 2021; Bezerra et al., 2020; Ramos et al., 2022). In the Araripe Basin, Marques et al. (2014) proposed that inversion resulted from far-field ENE-WSW directed horizontal maximum compressive stress. They concluded that this deformation is consistent with the formation of new oceanic crust in the South Atlantic to the east and the development of the Andes to the west, resulting in overall compression of the South America plate (Coblentz and Richardson, 1996; Marques et al., 2013).

According to Marques et al. (2014), this compression caused large-scale inversion of the initial high angle normal faults of the Araripe Basin (Fig. 1e) through oblique convergence and injection of soft material into these faults. By contrast, Peulvast and Bétard (2015) proposed that the present-day topographic elevation of the basin is due to regional uplift of the Borborema Province and the action of differential erosion (Fig. 1d). The Peulvast and Bétard (2015) scenario fits with the general absence of large-scale inversion of normal faults as seen on seismic sections from the Araripe Basin (Ponte and Ponte-filho, 1996, Rosa et al., 2023). However, on closer inspection, these seismic sections do in fact show a limited degree of normal fault inversion (Ponte and Ponte-filho, 1996; Cardoso, 2010; Rosa et al., 2023), and localized reverse faulting linked to basin inversion is observed in nearby basins of the same age as well (e.g., the Rio do Peixe Basin, Vasconcelos et al., 2021). As such, the exact mechanism causing inversion, and to what degree rift structures were reactivated in the Araripe Basin remains unclear, requiring further research with new approaches. One of these new approaches is the use of analogue modelling, which has shown to be a useful

tool to understand the evolution of inverted basins and the mechanisms involved in various settings (Brun and Nalpas, 1996; Nalpas et al., 1995; Panien et al., 2005a; del Ventisette et al., 2005, 2006; Marques and Nogueira, 2008; Pinto et al., 2010a; di Domenica et al., 2014; Jara et al., 2018; Zwaan et al., 2022b).

In this paper we therefore present the results of new [crustal-scale](#) analogue modeling experiments [completed](#) with a novel set-up, which are aimed at evaluating whether tectonic compression could have caused the inversion observed in the Araripe Basin. In our models we test the influence of orthogonal ( $\alpha=0$ ) or oblique ( $\alpha=45^\circ$ ) divergence, followed by either orthogonal or oblique convergence, as well as syn-rift sedimentation on initial basin development and on subsequent inversion structures. We then compare our model results with data from nature and propose an updated scenario for inversion of the Araripe Basin involving oblique inversion and the development of low-angle reverse faults outside the basin.



90 **Figure 1: a) Structural geology of the study area and present-day Araripe Basin (AB). [NE-SW striking rift-related structures \(in blue\)](#) and [Precambrian basement shear zones \(in black\)](#), modified after [Camacho and de](#)**

Oliveira e Sousa (2017); Note that most faults (in blue) in the Araripe Basin are covered by post-rift sediments and are interpreted from reflection seismic sections (Ponte e Ponte-Filho, 1996). NE-SW rift related structures (in blue) and Precambrian basement shear zones (in black), modified after Camacho and de Oliveira e Sousa (2017). PSZ: Patos Shear Zone. b) Schematic N-S section representing rift and post-rift formations in the Araripe Basin prior to inversion. c) Schematic representation of the Araripe Basin inversion model based on regional uplift followed by differential erosion proposed by Peulvast and Bétard (2015). d) Schematic representation of the Araripe Basin inversion model as a result of regional oblique convergence proposed by Marques et al. (2014).

95

## 100 2 Methods

### 2.1 Model set up

For this study of crustal-scale basin inversion processes, we used an experimental set-up involving two long mobile sidewalls, two rubber end walls (fixed between the mobile walls, closing the short model ends), and a base consisting of a mobile and a fixed base plate (Fig. 2a). We positioned a 5 cm thick block consisting of intercalated foam (1 cm thick) and Plexiglas (0.5 cm thick) bars above the base plates and between the long sidewalls (Fig. 2a,b). This foam/Plexiglas block, initially 36.5 cm wide, was compressed prior to adding the model materials in order to reach the initial width of 30 cm (Fig. 2a,b). Divergence of the mobile long sidewalls, achieved by high-precision computer-controlled motors, simulates an initial rifting phase inducing uniform orthogonal divergence into the overlying brittle and viscous model materials that represent the brittle upper crust and ductile lower crust, respectively. For orthogonal convergence during the subsequent inversion phase, the sidewalls are simply moved together again. During oblique divergence and oblique convergence, which we apply to account for possible different deformation kinematics during basin formation and inversion, such as proposed by e.g. Marques et al. (2014) and Rosa et al. (2023), additional lateral motion of one mobile base plate was applied (Fig. 2c). In order to localize deformation in our models, creating a graben during the initial rifting phase, we introduce a linear seed on the top of the viscous layer that was made from the same viscous material as used for the lower crustal layer (e.g., Le Calvez & Vendeville 2002; Molnar et al., 2019, 2020; Zwaan and Schreurs, 2017). This seed was a semi-cylindrical ridge with a c. 1 cm diameter, and was placed in the same position in each model (i.e. along the central axis of the model, Fig. 2a,b).

105

110

115

120

125

Our general model set-up has been regularly used for orthogonal and oblique rifting, and transpression models (Schreurs and Colletta, 1998, 2002; Zwaan and Schreurs, 2017; Zwaan et al., 2016, 2018a, 2020; Schmid et al, 2022a, b), but so far only Guillaume et al. (2022) have applied a similar foam-based set-up for basin inversion modelling, with the fundamental key difference that shortening in the convergence direction in their models was perpendicular to the divergence direction. Our model set-up design is also fundamentally different from previous basin inversion model set-ups involving base plates and/or sidewalls for orthogonal and oblique basin inversion, which tend to strongly localize model deformation along the base plate edges, or at the sidewalls, respectively (e.g. Brun and Nalpas, 1996; Nalpas et al, 1995, see also Zwaan et al. 2022b, and references therein for an extensive discussion on analogue basin inversion model set-ups).

130

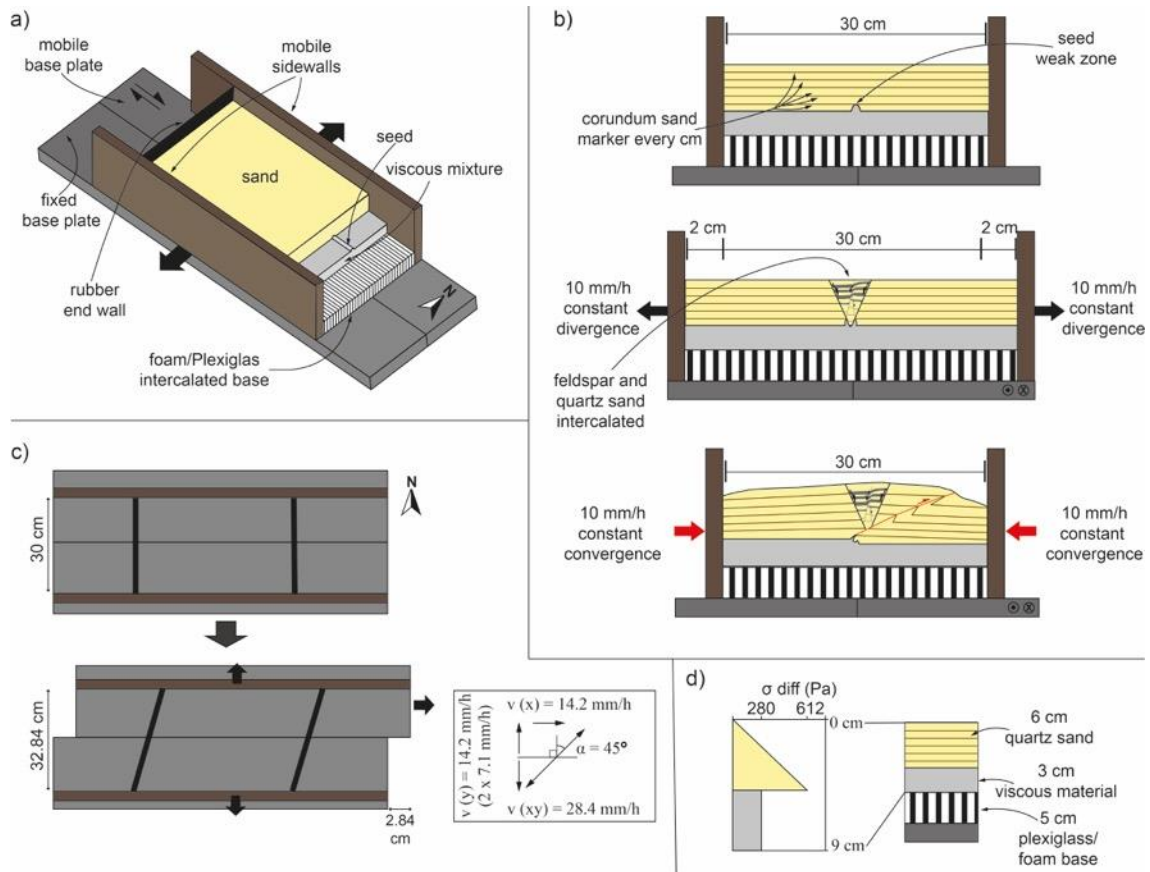


Figure 2: Experimental set-up adopted for this study. a) 3D cut-out view showing the brittle-viscous layers on top of the Plexiglas/foam base of the experiment (north arrow added for reference in the models). b) Schematic example of a sedimentation model run in 2D. c) Top view example of movement direction of the experimental apparatus used in this study (oblique divergence example, with definition of divergence and convergence obliquity as angle  $\alpha$ ). Note that angle  $\alpha$  is positive for dextral oblique divergence, as well as for sinistral oblique convergence. Vice versa, angle  $\alpha$  is negative for sinistral oblique divergence and for dextral oblique convergence). d) Schematic strength profile indicating the crustal setting represented in our models.

135

## 140 2.2 Materials

We utilized brittle and viscous analogue materials (material properties summarized in Table 1) to reproduce the brittle and ductile parts of the upper and lower crust in our experiments.

A 3 cm thick viscous layer served to replicate a 10 km thick lower crust. This material consists of a near-Newtonian ( $\eta = \text{ca. } 1.5 \cdot 10^5 \text{ Pa} \cdot \text{s}$ ;  $n = 1.05\text{-}1.10$ , Zwaan et al., 2018c) mixture of SGM-36 Polydimethylsiloxane (PDMS) and corundum sand ( $\rho_{\text{specific}} = 3950 \text{ kg/m}^3$ , <https://www.carloag.ch>). We mixed the components according to a 0.965: 1.00 weight ratio, resulting in a viscous mixture with a density of ca.  $1600 \text{ kg/m}^3$ .

We applied a 6 cm thick layer of fine quartz sand ( $\phi = 60\text{-}250 \mu\text{m}$  and  $\phi = 31.4\text{-}36.1^\circ$ , Zwaan et al. 2018a) sieved on top of the viscous layer, representing a 20 km brittle upper crust. The sand was flattened at 1 cm intervals with a scraper to avoid lateral variation in sand layer thickness during the model preparation. We sieved the sand from ca. 30 cm height to ensure a constant brittle layer density of ca.  $1560 \text{ kg/m}^3$  (e.g. Klinkmüller et al., 2016; Schmid et al., 2020).

150

We used layers of feldspar sand (grain size range = 100-250  $\mu\text{m}$  and  $\phi = 29.9\text{-}35^\circ$ , Zwaan et al., 2022c) intercalated with layers of quartz sand for sedimentary infill in order to provide a visual record of syn-rift units on sections (Fig. 2b). The sand application was done by hand, using a paper cone with an opening of 3 mm at the tip. The flux of sand was controlled by pressing the opening of the cone and we filled the graben up to the general model surface.

Furthermore, we added thin <1 mm thick marker intervals of fine corundum sand (grain size range = 88-125  $\mu\text{m}$ ) to the quartz sand layer, which allowed for the tracing of deformation in section view (Fig. 2b). These thin intervals were sieved in during the scraping intervals (every cm) and are not considered to have an impact on model evolution.

**Table 1: Materials properties**

<b>Granular materials</b>	<b>Quartz sand<sup>a</sup></b>	<b>Corundum sand<sup>b</sup></b>	<b>Feldspar sand<sup>b</sup></b>
Grain size range ( $\phi$ )	60-250 $\mu\text{m}$	88-125 $\mu\text{m}$	100-250 $\mu\text{m}$
Specific density ( $\rho_{\text{specific}}$ ) <sup>c</sup>	2650 kg/m <sup>3</sup>	3950 kg/m <sup>3</sup>	ca. 2700 kg/m <sup>3</sup>
Sieved density ( $\rho_{\text{sieved}}$ )	1560 kg/m <sup>3</sup>	1890 kg/m <sup>3</sup>	ca. 1300 kg/m <sup>3</sup>
Angle of internal peak friction ( $\phi_{\text{peak}}$ )	36.1°	37°	35°
Coefficient of internal peak friction ( $\mu_{\text{peak}}$ ) <sup>d</sup>	0.73	0.75	0.70
Angle of dynamic-stable friction ( $\phi_{\text{dyn}}$ )	31.4°	32.0°	29.9°
Coefficient of dynamic-stable friction ( $\mu_{\text{dyn}}$ ) <sup>d</sup>	0.66	0.62	0.58
Angle of reactivation friction ( $\phi_{\text{react}}$ )	33.5°	-	32.0°
Coefficient of reactivation friction ( $\mu_{\text{react}}$ )	0.66	-	0.62
Cohesion (C)	9 $\pm$ 98 Pa	39 $\pm$ 10 Pa	51 Pa
<b>Viscous material</b>	<b>Pure PDMS<sup>a,e</sup></b>	<b>PDMS/corundum sand mixture<sup>a</sup></b>	
Weight ratio PDMS : corundum sand	-	0.965 kg : 1.00 kg	
Density ( $\rho$ )	965 kg/m <sup>3</sup>	ca. 1600 kg/m <sup>3</sup>	
Viscosity ( $\eta$ )	ca. $2.8 \cdot 10^4$ Pa.s	ca. $1.5 \cdot 10^5$ Pa.s <sup>f</sup>	
Type <sup>f</sup>	Newtonian (n = ca. 1) <sup>g</sup>	near-Newtonian (n = 1.05-1.10) <sup>g</sup>	
<p>a Quartz sand, PDMS and viscous mixture characteristics after Zwaan et al. (2016; 2018a, 2018b)</p> <p>b Corundum sand characteristics after Panien et al. (2006)</p> <p>c Specific densities after Carlo AG (2022)</p> <p>d <math>\mu = \tan(\phi)</math></p> <p>e Pure PDMS rheology details after Rudolf et al. (2016)</p> <p>f Viscosity value holds for model strain rates &lt; <math>10^{-4}</math> . s<sup>-1</sup></p> <p>g Power-law exponent n (dimensionless) represents sensitivity to strain rate</p> <p>h Feldspar sand characteristics after Zwaan et al. (2022c)</p>			

### 2.3 Model parameters

For this study we completed two main series of four experiments each, and an initial series of reference experiments (Table 2). Series A contains our reference experiments that simulated the initial (orthogonal) rifting phase only, with and without syn-rift sedimentation. Series B explores the effects of basin inversion without syn-rift sedimentation. Series C tests the effects of syn-rift sedimentation during basin inversion. The initial rifting phase of our Series B and C basin inversion models involved either orthogonal or 45° oblique divergence (where obliquity is defined by angle alpha, i.e. the angle between the normal to the rift axis and the divergence direction, Fig. 2c). The subsequent phase of shortening involved either orthogonal or (-)45° oblique convergence (see details in Table 2). The experiments ran for 2 hours with 40 mm of divergence (at 20 mm/h) and another 2 hours with 40 mm of convergence, except for models B3 and C3 since the initial oblique opening did not generate sufficient space for a subsequent orthogonal convergence component of 40 mm. Therefore, total convergence in models B3 and C3 was 28 mm (over 85 min) instead, which was however sufficient convergence to establish well-developed inversion features.

We implemented syn-rift sedimentation in 5 of our experiments (in Model A2 and in models C1-4), by halting the machine every 15 min (8 sedimentary intervals in total) and filling the accommodation space by hand (pouring), with feldspar and quartz sand in alternating intervals (Fig. 2b). The two experiments with oblique rifting have only 7 sedimentation intervals because after the first 15 minutes, insufficient accommodation space was available, requiring us to start the first sand filling after 30 minutes instead. [In each model, the final sedimentation interval after the end of rifting generated a nearly flat model topography prior to inversion \(Fig. 1b\).](#)

**Table 2: Parameters of analogue models performed in this study**

Model Series	Model Name	Direction and velocity of divergence/convergence				Sedimentation	Sections made
		Phase 1 (40 mm of divergence)		Phase 2 (40 mm of convergence)			
		Direction (angle $\alpha$ )	Velocity (v) mm/h	Direction (angle $\alpha$ )	Velocity (v) mm/h		
<b>Series A Reference rifting models</b>	A1	0°	20	-	-	No	Yes
	A2	0°	20	-	-	Yes	Yes
<b>Series B Rifting and inversion without sedimentation</b>	B1	0°	20	0°	20	No	Yes*
	B2 <sup>#</sup>	0°	20	-45°	20	No	No
	B3 <sup>§</sup>	45°	20	0°	20	No	No
	B4	45°	20	45°	20	No	No
<b>Series C Rifting and inversion with sedimentation</b>	C1	0°	20	0°	20	Yes	Yes
	C2 <sup>#</sup>	0°	20	-45°	20	Yes	Yes
	C3 <sup>§</sup>	45°	20	0°	20	Yes	Yes
	C4	45°	20	45°	20	Yes	Yes

\* Sections not used in this paper, presented in the supplementary material

---

# Models with initial orthogonal divergence underwent dextral inversion ( $\alpha = -45^\circ$ ) due to technical limitations of our model apparatus. However, one can simply mirror the result to obtain the sinistral inversion equivalent ( $\alpha = 45^\circ$ )

\$ Models with reduced inversion time due to the oblique divergence with reduced orthogonal divergence component.

## 2.4 Scaling

190 Model scaling is important to guarantee that experiments completed in the laboratory are representative of their counterparts in nature. For the brittle materials, the main parameter is the angle of internal friction ( $35^\circ$ - $37^\circ$ ), which is similar to internal friction angle values found in the upper crust ( $31^\circ$ - $38^\circ$ , Byerlee, 1978, Table 3). In order to scale the viscous material, we must consider its strain rate-dependent rheology. The stress ratio between model and nature ( $\sigma^*$ , convention:  $\sigma^* = \sigma_{\text{model}} / \sigma_{\text{nature}}$ ) is calculated as follows:  $\sigma^* = \rho^* \cdot h^* \cdot g^*$ , where  $\rho^*$ ,  $h^*$  and  $g^*$  represent density, length, and gravity ratios, respectively (Hubbert, 1937; Ramberg, 1981). Combined with the viscosity ratio ( $\eta^*$ ), the stress ratio yields the strain rate ratio  $\dot{\epsilon}^*$  (Weijermars and Schmeling, 1986):  $\dot{\epsilon}^* = \sigma^* / \eta^*$ . Subsequently, the velocity and time ratios ( $v^*$  and  $t^*$ ) are derived from the strain rate ratio:  $\dot{\epsilon}^* = v^* / h^* = 1 / t^*$ . We adopt a relatively high lower crustal viscosity of ca.  $5 \cdot 10^{21}$ , representing a typical early magma-poor rift system (e.g. Buck, 1991). Thus, one hour in our model represents ca. 1.3 Myr in nature, and 20 mm/h of divergence/convergence in the model embodies a realistic deformation velocity of ca. 5 mm/yr in nature. The scaling parameters are presented in Table 3.

The dynamic similarity of the model and natural example can also be examined. Firstly, the dynamic similarity between the model brittle layer and its upper crustal equivalent can be determined through the ratio  $R_s$  between the gravitational stress and the cohesive strength or cohesion  $C$  (Ramberg, 1981; Mulugeta, 1988):  $R_s = \text{gravitational stress} / \text{cohesive strength} = (\rho \cdot g \cdot h) / C$ . The 9 Pa cohesion in the sand and a natural cohesion of 5 MPa for upper crustal rocks, gives us a  $R_s$  of 102 and 110 for model and nature, respectively. Secondly, the dynamic similarity between our viscous material and lower crust equivalent is derived from the Ramberg number  $R_m$  (Weijermars and Schmeling, 1986):  $R_m = \text{gravitational stress} / \text{viscous strength} = (\rho \cdot g \cdot h^2) / (\eta \cdot v)$ , and both have the value of 68. We consider our models properly scaled [for simulating crustal-scale inversion processes](#) since their  $R_s$  and  $R_m$  values are similar to their natural equivalent.



Table 3: Scaling parameters

		<b>Model</b>	<b>Nature</b>
<b>General parameters</b>	Gravitational acceleration (g)	9.81 m/s <sup>2</sup>	9.81 m/s <sup>2</sup>
	Divergence velocity (v)	5.6 · 10 <sup>-6</sup> m/s	1.7 · 10 <sup>-10</sup> m/s
<b>Brittle layer</b>	Material	Quartz sand	Upper crust
	Peak internal friction angle	35°-37°	31-38°
	Thickness (h)	6 · 10 <sup>-2</sup> m	2 · 10 <sup>4</sup> m
	Density	1560 kg/m <sup>3</sup>	2800 kg/m <sup>3</sup>
	Cohesion (C)	9 Pa	5 · 10 <sup>6</sup> Pa
<b>Viscous/ductile layer</b>	Material	PDMS/corundum sand mixture	Lower crust
	Thickness (h)	3 · 10 <sup>-2</sup> m	1 · 10 <sup>4</sup> m
	Density	1600 kg/m <sup>3</sup>	2900 kg/m <sup>3</sup>
	Viscosity	1.5 · 10 <sup>5</sup> Pas	1 · 10 <sup>21</sup> Pas
<b>Dynamic scaling values</b>	Brittle stress ratio (R <sub>s</sub> )	102	110
	Ramberg number (R <sub>m</sub> )	68	68

215

## 2.5 Model monitoring and analysis

The experiments were primarily monitored through time-lapse photographs of the model surface, taken every minute for the duration of the model run. One central camera (Nikon D810, 36 MPx) provided map view pictures, while two obliquely oriented cameras (D810, 36 MPx) were positioned on both sides of the central one to provide stereoscopic imagery. The central camera was controlled using Nikon Camera Control Pro software and cameras for stereoscopic imagery were remotely triggered by passing on the signal from the central camera via an ESPER Triggerbox (Schmid et al., 2022).

To facilitate the first order surface deformation analysis, we sieved a thin grid (4 by 4 cm) of corundum sand on the model surface. We furthermore sprinkled the model surface with coffee powder to provide markers for later Digital Image Correlation (DIC) analysis. For the models involving syn-rift sedimentation, a fine layer (< 1 mm) of quartz sand was sieved on the top of the experiment at the end of rifting phase to create a blank surface for a new grid and new coffee markers, allowing for optimal tracing of deformation during the inversion phase. Note that we defined a North reference in the models in order to facilitate the description of our model results (Fig. 2)

To quantify and visualize the surface deformation evolution of the experiments, we applied a detailed analysis of the time-lapse photographs through DIC techniques (e.g. Adam et al., 2005; Boutelier et al., 2019; Marshak et al., 2019; Zwaan et al., 2021; Schmid et al., 2022). The DIC analysis was performed by comparing top view images of subsequent time steps using LaVision's DaVis software (version 10.2). We used a calibration plate with a cross pattern of known dimensions as a reference to unwarp and rectify images and scale calculated displacements. Maximum and minimum normal strains are defined as the magnitude of the largest (i.e., stretching) and smallest (i.e., shortening) axes of the strain ellipse, and are independent of reference frame (e.g. Broerse et al., 2021). It is therefore a suitable marker to quantify extension and shortening in our experiments, respectively.

To reconstruct the model topography in detail, we used the pair of high-resolution oblique photographs for selected time steps. Agisoft Photoscan photogrammetry software served to merge this pair of synchronous photographs, using marked coordinates in the experiment for geo-referencing, and to create digital elevation models (DEMs) at the end of both the rifting and inversion phases. The DEMs, shown in map view, as well as the extracted topography profiles over time, are combined with the [DICPIV](#) results for a complete interpretation of model surface evolution (e.g. Maestrelli et al., 2020; Zwaan et al., 2022a).

Finally, sections were made to reveal the internal structures of the models at the end of the model run (at the end of the rifting phase for Series A models, and after inversion for Series B and C). In order to produce these sections, we added water with soap at the edges of the model until the sand was saturated and stable, and cut 6 sections orthogonal to the model axis, each 10 cm apart. Pictures were taken for analysis of internal structures and quantification of subsidence. The sections of the reference models (Series A) provide insights into graben structures prior to inversion.

### 3 Results

255 The results of our model analysis are presented in summary figures for each experiment (Figs. 3-8). We show the incremental maximum and minimum normal strain from the DIC analysis for the early stage (first 30 minutes) and end stage of each phase (85-120 minutes interval), topography maps for the end of each deformation phase, and topographic profiles over 30 minutes increments. Model sections are presented for Series A and C.

260

#### 3.1 Series A – Reference models

The Series A models provided a reference for the Series B and C analysis. These models had a constant orthogonal divergence direction ( $\alpha = 0^\circ$ ) and a divergence velocity of 20 mm/h (Fig. 3). In Model A1 no sedimentation was applied during rifting, whereas in Model A2, eight phases of syn-rift sedimentation were applied at 15 minutes intervals.

265

##### 3.1.1 Orthogonal rift without syn-rift sedimentation - Model A1

Deformation in Model A1 localized in the first 30 minutes (Fig. 3a), with two graben boundary faults rooting in the viscous seed (Fig. 3i<sub>I-III</sub>) accommodating extension in one E-W striking graben. Towards the end of the rifting phase ( $t = 120$  min, Fig. 3b), a second-generation intra-graben fault developed between the two conjugate graben boundary faults. The strain analysis indicates higher strain values in the southern graben border fault and within the second-generation intra-graben fault (Fig. 3b). However, the northern graben border fault also remained active until the end of the experiment (Fig. 3b). Section view shows drag folds associated with the northern and southern graben boundary faults (Fig. 3i). The final topography profiles (Fig. 3d;  $t = 60$  min, 90 min and 120 min) show a v-shaped depression on the southern side of the graben floor. This topographic feature can be related to the drag fold of the southern graben block seen in section view (Fig. 3i<sub>II</sub>), indicating that the drag fold initiated after the first hour of experiment and continued evolving until the end of the rifting phase. In section II (Fig. 3i<sub>II</sub>), we measured graben width between the two master faults bounding the grabens and the value is 56.2 mm. To measure the total fault offset, we used the uppermost corundum sand marker that showed a total of 19.2 cm of subsidence.

270

275

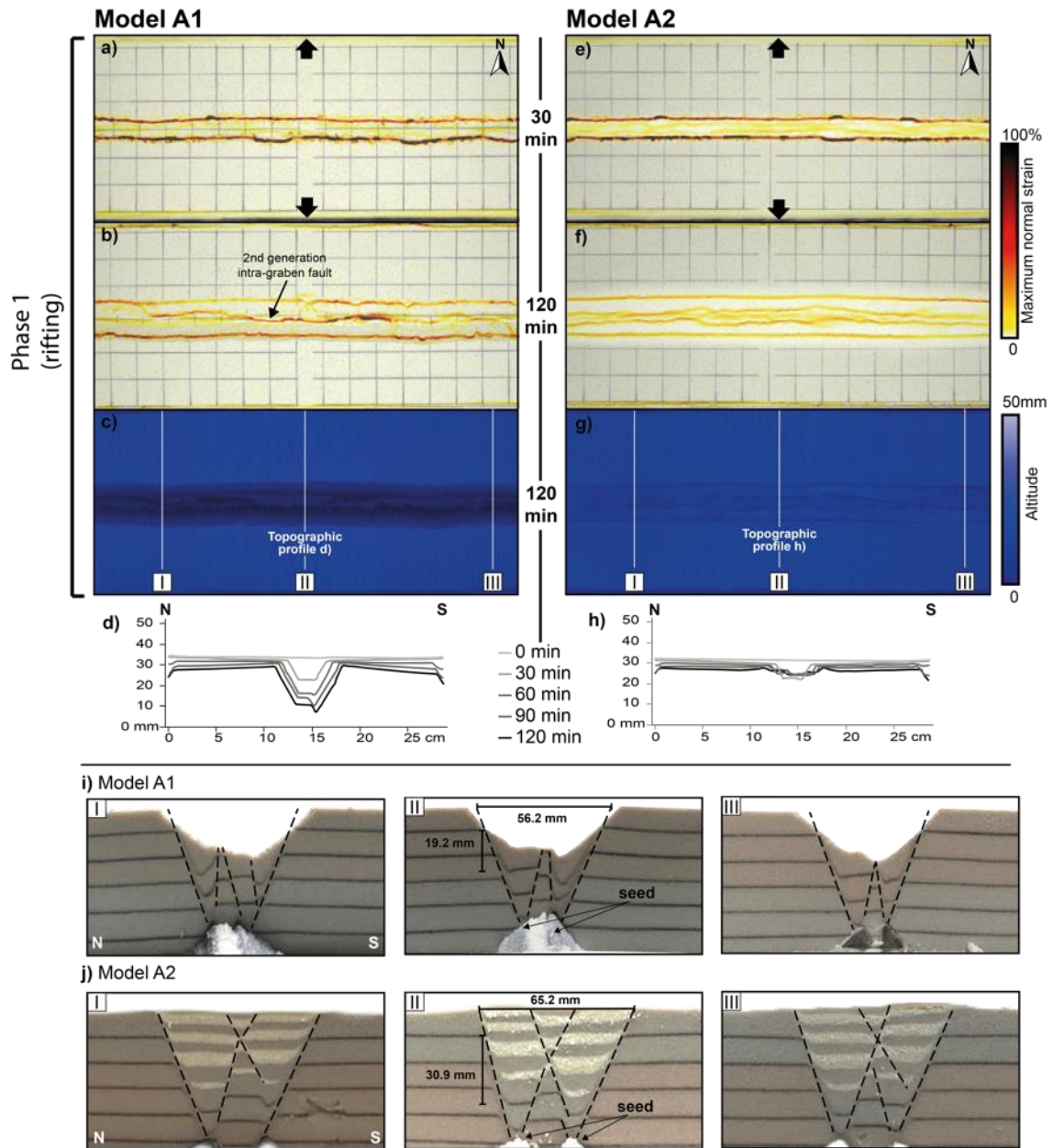
280

##### 3.1.2 Orthogonal rifting with syn-rift sedimentation – Model A2

In the early rifting stages of Model A2 ( $t = 30$  min), strain analysis shows deformation concentrating at the graben boundary faults (Fig. 3e). However, during these early rifting stages, the maximum normal strain values are lower inside the graben (Fig. 3e,f) than observed in Model A1 (Fig. 3a,b). Towards the end of the model run, strain was homogeneously distributed between the boundary faults and the set of conjugate faults in the center of the graben (Fig. 3f,j). Syn-rift sedimentation in Model A2 (Fig. 3j) caused an increase of graben width and subsidence compared to rifting without sedimentation in Model A1 (Fig. 3i): the offset of the first corundum sand marker shows a difference of ca. 1 cm between models A1 (19.2 mm; Fig. 3i<sub>II</sub>)

285

290 and A2 (30.9 mm; Fig. 3j<sub>ii</sub>), and the graben structure was ca. 1 cm wider in Model A2 (65.2 mm) than in Model A1 (56.2 mm).



295 | **Figure 3: Evolution of deformation during rifting for models A1 (no sedimentation) and A2 (with sedimentation).** a), b), e) and f) display top view maximum normal strain results for early and late-stage rifting, respectively, c) and g) show top views of digital elevation models at the end of rifting. d) and h) Topographic profiles for every 30 minutes of rifting. **Vertical exaggeration = 4.** Note that topography is shown prior to syn-rift sedimentation for that interval. i-j) Sections for Model A1 and Model A2, respectively. Section locations are indicated in (c) and (g). Graben geometry measurements are indicated in the middle sections (i<sub>ii</sub> and j<sub>ii</sub>).

300

### 3.2 Series B – inversion without [syn-rift](#) sedimentation

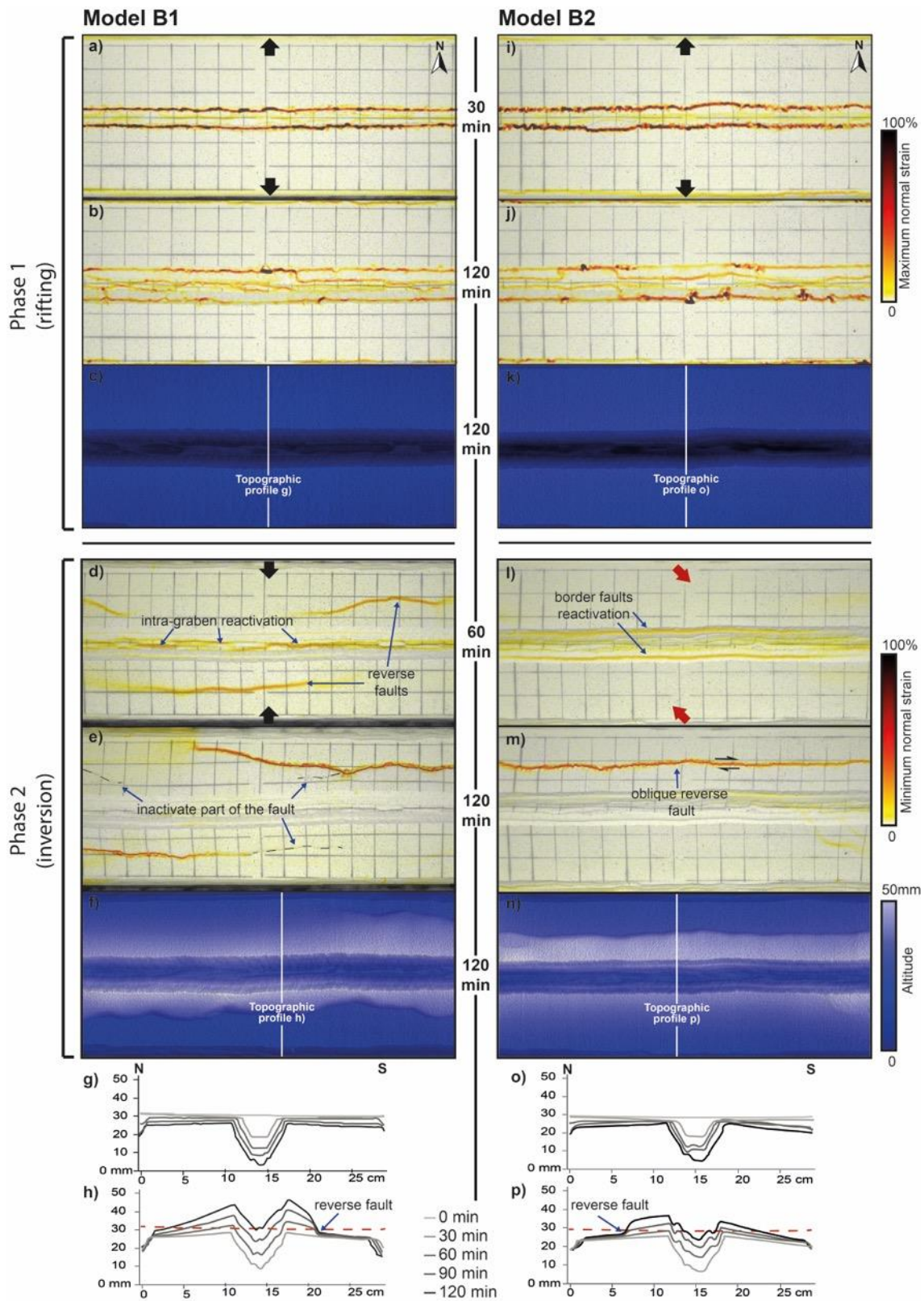
305 Here we show the results for the Series B models that underwent two deformation phases (rifting and inversion) but without syn-rift sedimentation. We first present models B1 and B2 that involved orthogonal rifting, followed by models B3 and B4 with oblique rifting. These model pairs subsequently underwent either orthogonal or oblique inversion.

#### 310 3.2.1 Orthogonal rifting followed by orthogonal (Model B1) or oblique (Model B2) inversion

The results from models B1 and B2 show very similar outcomes at the end of phase 1 and are also very similar to reference Model A1 (Figs. 3a-b; 4a-b and i-j). Early rifting ( $t = 30$  min, Fig. 4a and i) localized more strain along the graben normal faults than in the later rift phase as during the late rift stage ( $t = 120$  min, Fig. 4b and j), strain was distributed between the graben boundary faults and the intra-graben faults. 315 Topography analysis (Fig. 4c, g, k and o) shows a maximum graben subsidence of ca. 20 mm in both models.

After the first 60 minutes of orthogonal inversion, Model B1 localized strain both along the intra-graben faults and along new reverse faults on both sides of the graben (Fig. 4d). Towards the end of the model run, most parts of the southern reverse fault became relatively inactive while the northern reverse fault grew and 320 localized higher strain (Fig. 4e). During the final stage ( $t = 120$  min), also the intra-graben faults had become inactive (Fig. 4e). The areas immediately adjacent to the north and south of the graben were uplifted, while the floor of the inverted graben reached the same elevation as the pre-rift surface (Fig. 4f, h).

After the first 60 minutes of oblique inversion in Model B2, strain was localized along the graben boundary faults (Fig. 4l) showing direct reactivation of the original graben faults only, in clear contrast to the 325 orthogonal inversion of Model B1 (Fig. 4d). At the end of Phase 2, however, a single oblique reverse fault had appeared at the model surface grid, north of the graben, while all previous rift related faults were inactive (Fig. 4m). The final topography data show a significantly higher maximum elevation than the pre-rift surface of ca. 15 mm in orthogonal inversion Model B1 (Fig. 4f, h), while the oblique inversion Model B2 (Fig. 4n, p) had ca. 7 mm higher elevation than the pre-rift surface.



330

335

Figure 4: Evolution of deformation during rifting and inversion for models B1 and B2 (without sedimentation). a, b) and i-j) Top view maximum normal strain results for early and late-stage rifting, respectively. c, k) Digital elevation models at the end of rifting. d, e) and l, m) Top view minimum normal strain results for early and late-stage inversion, respectively. f, n) Top view of digital elevation model at the end of inversion. g, o) Topographic profiles for every 30 minutes of rifting. h, p) Topographic profiles for every 30 minutes of inversion. Vertical exaggeration = 4. The dashed red horizontal line indicates the initial surface level at the start of the model run.

### 3.2.2 Oblique rifting followed by orthogonal (Model B3) or oblique (Model B4) inversion

340 Oblique rifting ( $\alpha = 45^\circ$ ) of models B3 and B4 resulted in the development of two bands of *en échelon* normal faults bounding an E-W striking graben after the first 30 minutes of deformation (Fig 5a,i). At the end of Phase 1, the strain results show that these *en échelon* faults had become interconnected, forming through-going, E-W striking graben-bounding normal faults, connected by oblique, WNW-ESE trending, lower strain zones within the graben (Fig. 5b,j).

345 After 60 minutes of orthogonal inversion, Model B3 showed the formation of a new straight fault along the central axis of the graben and the development of a new reverse fault south of the graben (Fig. 5d,e). By the end of the inversion phase, after 120 minutes, the reverse fault remained active while the fault in the centre of the graben became less active, with some parts being completely inactive (Fig. 5e). Uplift was more prominent in the area between the reverse fault and the graben, whereas in the northern part of the model a more widespread uplift was recorded (Fig. 5f, g).

350 After 60 minutes of oblique inversion in Model B4, the oblique low strain zones within the graben were partially reactivated, while a significant portion of the deformation localized in a new reverse fault to the north of the graben, and deformation started to localize in the southern area of the model as well (Fig. 5l). After 120 minutes of inversion, the northern reverse fault became almost completely inactive, and deformation localized on the southern reverse fault (Fig. 5m). The map view grid analysis shows the oblique movement along the reverse faults (Fig. 5m). Rift faults experienced only minor reactivation and became almost completely inactive by the end of the inversion phase (Fig. 5m; 120 minutes). The topography profiles indicate uplift of the rift structures (17 mm elevation of the graben floor) and the new reverse faults on both sides of it (Fig 5p), and while the northern reverse fault became inactive, distributed uplift affected the northern part of the model (Fig. 5p). Along the topographic profile, the maximum uplift away from the reverse faults was 5 mm in the north (where the fault became inactive) and 2 mm in the south.

360

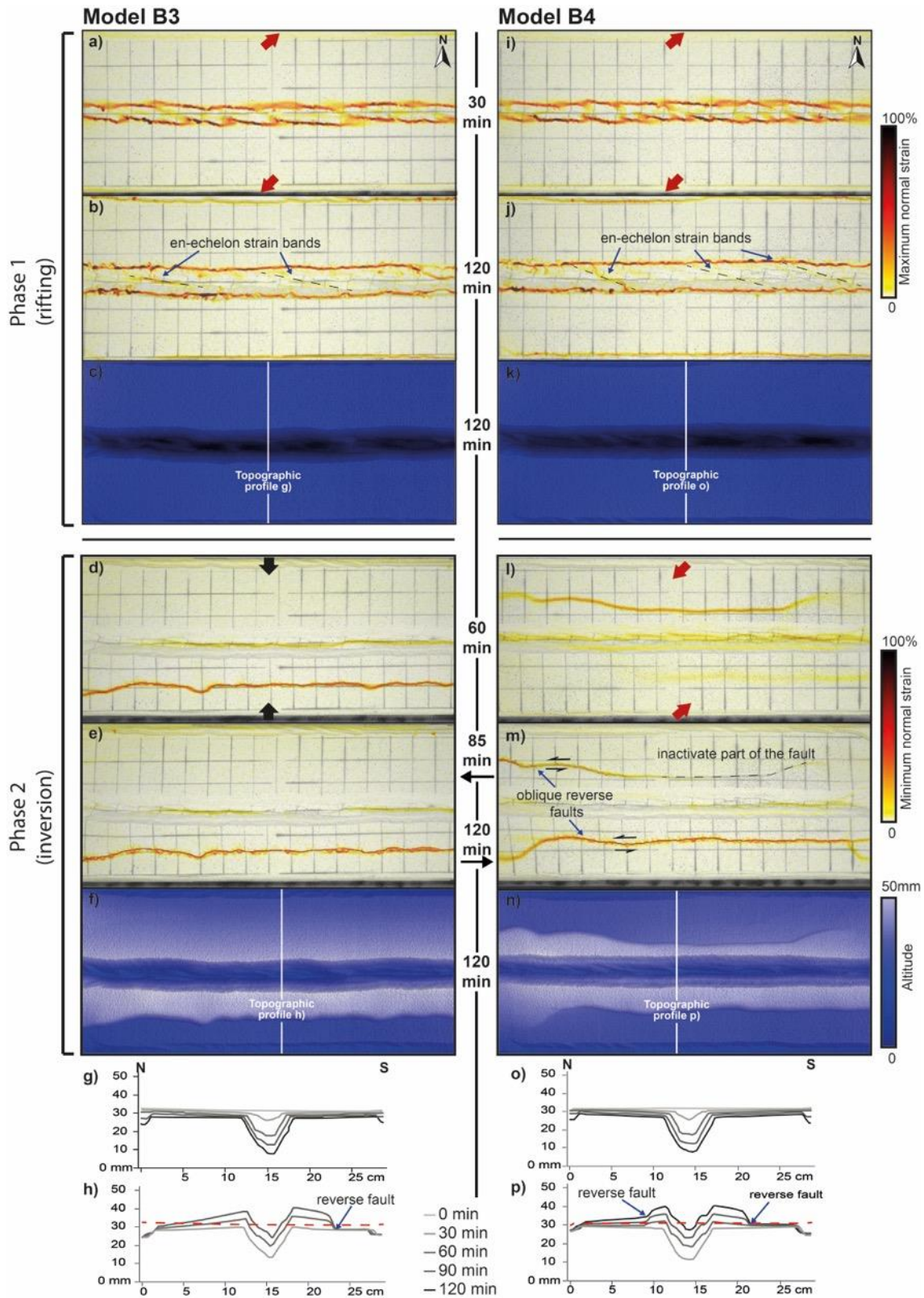


Figure 5: Evolution of deformation during rifting and inversion for models B3 and B4. Top view maximum normal strain results for early and late-stage rifting, respectively. c, k) Digital elevation models at the end of rifting. d, e) and l, m) Top view minimum normal strain results for early and late-stage inversion, respectively. f, n) Top view of digital elevation model at the end of inversion. g, o) Topographic profiles for every 30 minutes of rifting. h, p) Topographic profiles for every 30 minutes of inversion. **Vertical exaggeration = 4**. The dashed red horizontal line indicates the initial surface level at the start of the model run. Note that Model B3 has a reduced inversion time of 85 minutes instead of 120 minutes, as indicated in the figure.



### 370 3.3 Series C – inversion with syn-rift sedimentation

Here we present the results for our Series C models with the rifting phase divided in 8 sedimentation intervals of 15 minutes each, with 20 mm/h of displacement during both the rifting and subsequent convergence phases. The results are presented in pairs according to the models' initial divergence direction (orthogonal and oblique, respectively) (Figs. 6, 8).

375

#### 3.3.1 Orthogonal rifting with sedimentation followed by orthogonal (Model C1) or oblique (Model C2) inversion

380 The early stages of rifting of both models C1 and C2 resulted in high strain localization at the graben boundary faults and lower strain rates inside the graben (Fig. 6a,i). During later rifting stages, the maximum normal strain values were lower along the graben boundary faults and instead rather evenly distributed among all faults within the graben (Fig. 6b,j). These results for the early and late stages of rifting show great similarity to the results from Model A2 (Fig. 3e,f). Section thickness measurements from each of the 15 minutes syn-rift sedimentation intervals (I1-I8), indicate a progressive increase of subsidence in the first two sedimentation intervals (up to 8 mm/interval, inset in Fig. 7a<sub>i</sub>; I1 to I3). From interval I4 to I8, we 385 observed a decrease in the subsidence rate (down to ca. 4 mm/interval, inset in Fig. 7a; I4-8).

Orthogonal inversion in Model C1 concentrated deformation on a new reverse fault at the southern part of the model (Fig. 6d-e). Strain data show localization along this reverse fault, while no reactivation is visible in the inherited rift structures. In section view (Fig. 7a<sub>1,II</sub>) it becomes clear that the whole graben structure was uplifted by the reverse fault while the model surface was folded. The section shows that the reverse 390 fault, in fact a ca. 1 cm thick shear zone by the end of the model run, was seeded in the viscous layer, which itself was also thickened (most probably already during rifting as seen in sections from models A1 and A2, Figs 3i, j, 7a).

Compared to orthogonal inversion Model C1, oblique inversion in Model C2 shows a different effect on the reactivation of previous rift structures (Fig. 6l-m). We observed minor reactivation of the previously 395 formed graben-bounding normal faults during the subsequent oblique inversion phase, and main strain localization along newly formed reverse faults in the NW and SE quadrants, connected by strain localization zones parallel to the inversion direction. Our topography analysis shows a small (ca. 2 mm) pop-up structure related to minor inversion of the graben border faults (Fig. 6n,p), with a small dextral strike-slip component visible on the surface grid as well (Fig. 6m). In section view, the newly formed reverse faults were in fact 400 thick (ca. 1 cm) shear zones in those locations where only one of them developed, whereas the shear zones were thinner (< 5 mm) when multiple reverse faults developed (Fig. 7b).

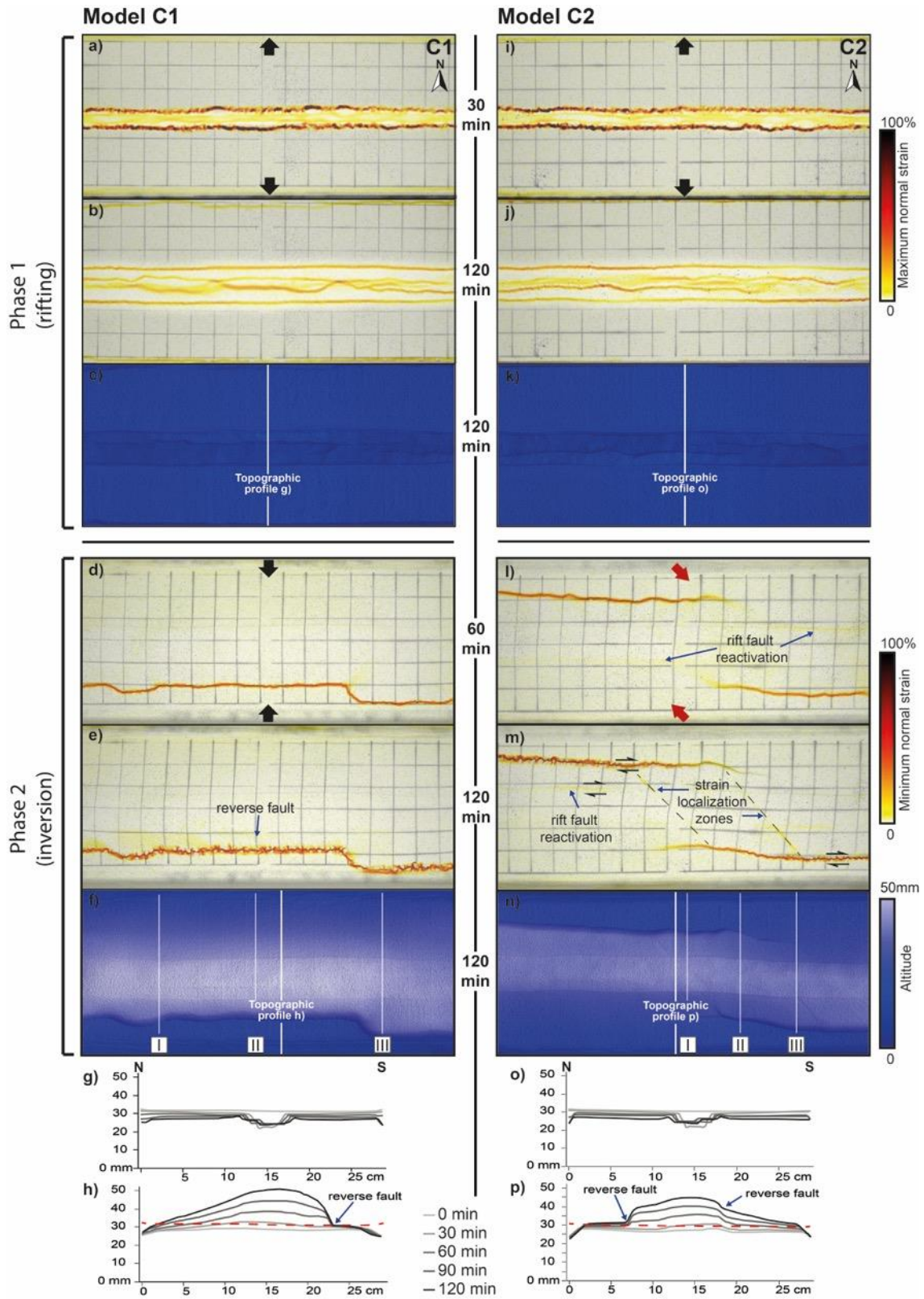
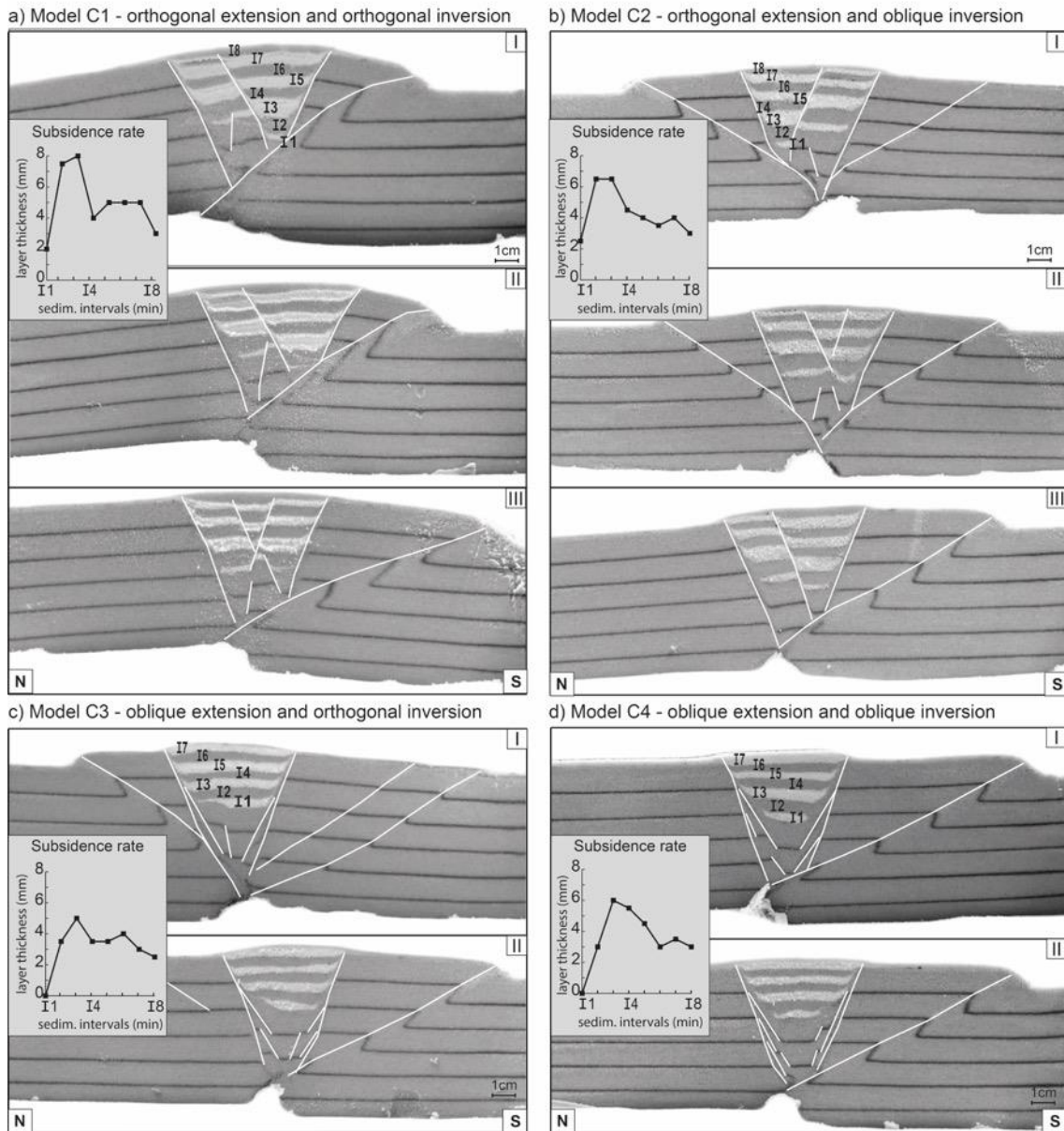


Figure 6: Evolution of deformation during rifting and inversion for models C1 and C2. a, b) and i-j) Top view maximum normal strain results for early and late-stage rifting, respectively. c, k) Digital elevation models at the end of rifting. d, e) and l, m) Top view minimum normal strain results for early and late-stage inversion, respectively. f, n) Top view of digital elevation model at the end of inversion. g, o) Topographic profiles for every 30 minutes of rifting. h, p) Topographic profiles for every 30 minutes of inversion. **Vertical exaggeration = 4.** Topography is shown prior to syn-rift sedimentation for that interval, and the dashed red horizontal line indicates the initial surface level at the start of the model run.



415 **Figure 7:** a), b), c) and d) Sections of experiments with sedimentation and measurements on models showing the influence of extension obliquity on sedimentation and subsidence rate. Section locations are shown in Figs. 5 and 8. Syn-rift sedimentation units always start with feldspar sand (white) and are divided into 8 intervals of 15 minutes of extension, except for the oblique divergence models C3 and C4, where I1 and I2 are represented in the same unit. I1 = 15 min, I2 = 30 min, I3 = 45 min, I4 = 60 min, I5 = 75, I6 = 90 min, I7 = 105 min, I8 = 120 min (after the initiation of rifting). Section orientations are indicated at the bottom section of each model.

### 3.3.2 Oblique rifting with sedimentation followed by orthogonal (Model C3) or oblique (Model C4) inversion

Models C3 (Fig. 8a) and C4 (Fig. 8i) developed clear *en échelon* graben boundary faults after the first 30 minutes of oblique rifting, thus showing results similar to models B3 and B4 (Fig. 5b, i). Over the  
425 subsequent 1.5 hours of rifting, the *en échelon* faults evolved into two main E-W graben boundary faults,  
but some faint [late-stage](#) *en échelon* strain bands remained active within the graben (Fig. 8b,j). Topography analysis shows that vertical subsidence in the first 30 minutes was lower than during the subsequent 30 minutes phases (2 mm/interval vs. 4.8 mm/interval, Figs. 7c, d). Subsidence was indeed slower in models C3 and C4 when compared to models C1 and C2: it took 30 minutes of oblique rifting (two 15 minutes  
430 intervals) to create accommodation space for sedimentation, while the first 15 minutes of orthogonal rifting in models C1 and C2 created enough subsidence for applying a sedimentation interval. Model C3 and C4 (Fig. 7c,d) did not develop the intra-graben normal faults seen in models C1 and C2 (Fig. 7a,b).

Orthogonal inversion in Model C3 created initial reverse faulting in the north and SE of the models, but without graben boundary fault reactivation (Fig. 8d). By the end of the experiment (Fig. 8e), after 85  
435 minutes, the northern reverse fault became completely inactive while the southern one grew laterally (westward), remaining active. Topography analysis shows uplift limited by the reverse faults on both sides of the model (Fig. 8f,h). In section view, there is an alternation between northern (Fig. 7c<sub>I</sub>) and southern (Fig. 7c<sub>II</sub>) reverse fault activity, and we also observe that reverse faults with larger offsets had an increased thickness.

440 The oblique inversion in Model C4 (Fig. 8l-m) is predominantly accommodated by a new reverse fault in the south, with limited reactivation of the rift structures. Topography data show additional uplift in the graben in contrast to the orthogonal inversion structures in Model C3 (Fig 8f). The topographic profiles (Fig. 8p) indicate limited inversion of the graben boundary faults, starting after the first hour and continuing until the end of the experiment.

445 The sections of models C3 and C4 (Fig. 7c,d) revealed that the reverse fault nucleated in the seed at the base of the graben, and developed into a ca. 1 cm thick shear zone. Section II from orthogonal inversion Model C3 (Fig. 7c) shows the presence of a reverse fault north of the graben, seeding 2 cm below the surface, with no clear link to the previous rift faults or to the viscous material at the base of the graben, which is in contrast to the other reverse faults visible in Fig. 7. However, in map view (Fig. 8d-f), it is  
450 shown that this is in fact the tip of the same reverse fault present in Section I of Model C3 (Fig. 7c)

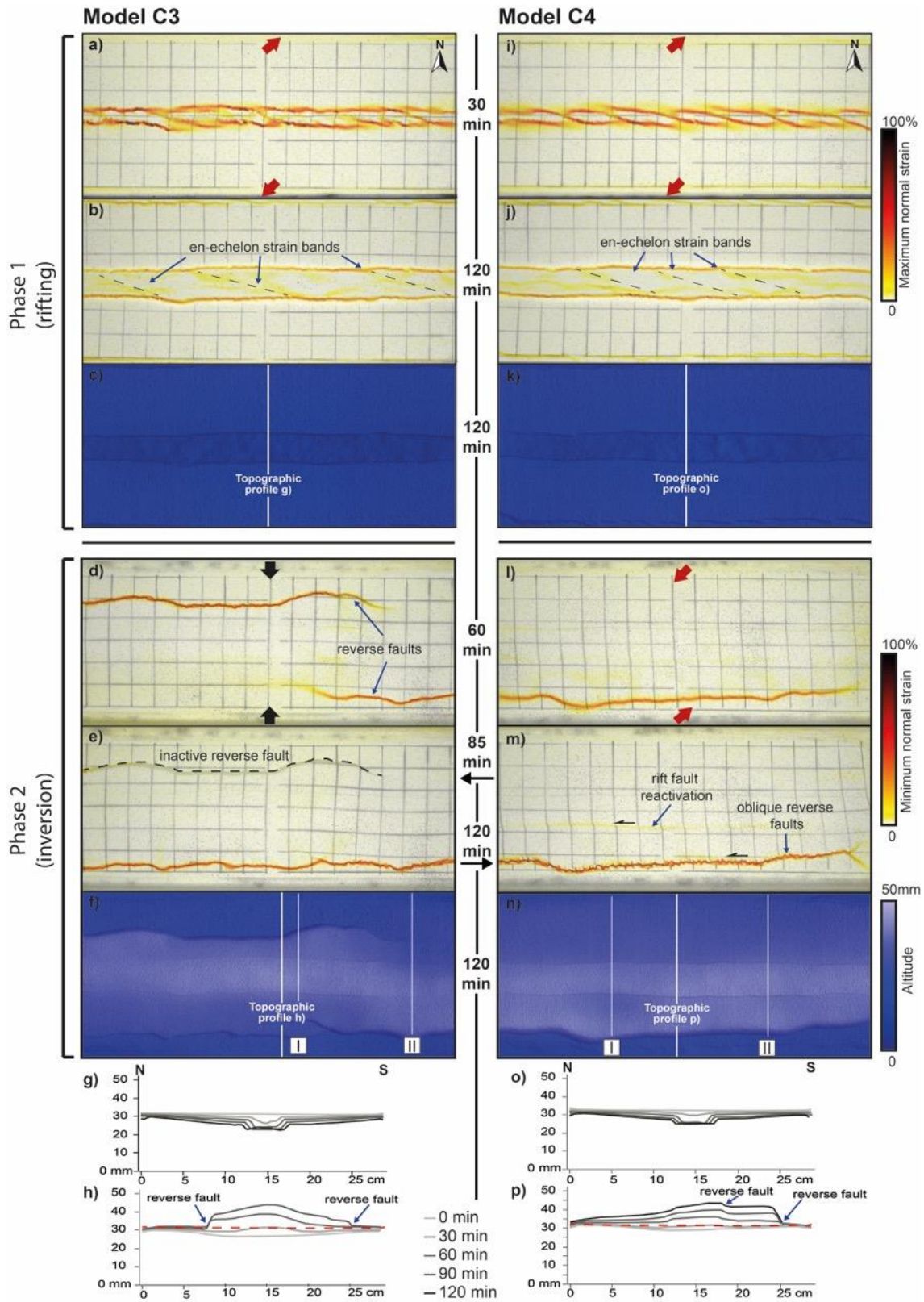


Figure 8: Evolution of deformation during rifting and inversion for models C3 and C4. a, b) and l-j) Top view maximum normal strain results for early and late-stage rifting, respectively. c, k) Digital elevation models at the end of rifting. d, e) and l, m) Top view minimum normal strain results for early and late-stage inversion, respectively. f, n) Top view of digital elevation model at the end of inversion. g, o) Topographic profiles for every 30 minutes of rifting. h, p) Topographic profiles for every 30 minutes of inversion. **Vertical exaggeration = 4.** Topography is shown prior to syn-rift sedimentation for that interval, and the dashed red horizontal line indicates the initial surface level at the start of the model run. Note that Model C3 has a reduced inversion time of 85 minutes instead of 120 minutes, as indicated in the figure.

## 4 Discussion

### 4.1 Summary and comparison to previous models

The modeling results, presented in two schematic overview figures (Figs. 9 and 10), show how imposed kinematics and the presence of syn-rift sedimentation affects initial basin evolution and subsequent inversion.

#### 4.1.1. Rifting phase

The overview of the rifting phase without sedimentation (Fig. 9a and b) depicts the general differences in graben structure as a result of divergence direction (orthogonal or oblique). A different divergence direction resulted in different initial graben structures. However, at the final stage of rifting, the graben geometries formed during orthogonal and oblique rifting were very similar (Fig. 9). The main difference occurs within the graben, where parallel pairs of conjugate normal faults formed due to orthogonal divergence, whereas oblique divergence resulted in *en échelon* structures. Furthermore, oblique divergence caused a decrease in graben width compared to the orthogonal rifting models, due to an increase in boundary fault dip, as also described in previous modelling studies (Tron & Brun 1991; Zwaan and Schreurs, 2016; Zwaan et al., 2018a) (Figs. 3 and 4). This reduction in width and increase in fault angle is caused by the strike-slip component accommodating deformation in oblique rifting settings.

The syn-rift sedimentation models (Fig. 10a and b) showed the same initial difference in orthogonal and oblique divergence as the models without sedimentation. The oblique divergence models resulted not only in a narrower graben at the end of the extension phase, but also in a reduction of the final total subsidence observed in section (Fig. 7). A narrower graben forming during oblique rift evolution led to smaller loads of sedimentation, consequently there was less graben floor subsidence. However, orthogonal and oblique rifting produced a very similar subsidence evolution in response to the syn-rift sedimentation (Fig. 7). The first subsidence interval (I1) was always the smallest, while the subsequent three intervals (I2 to I4) accommodated more subsidence, and from this moment on, sedimentary intervals started thinning again until the last interval (I8). This initial subsidence rate increase likely occurred because the increase in sedimentary load over time enhanced subsidence. However, the reason why we observe a subsidence decline after sedimentation interval I4 remains unclear.

Overall, concerning the total subsidence in models with and without syn-rift sedimentation, we observe that subsidence in the former case was significantly higher while the rift boundary faults remained active for a longer period of time as well. Zwaan et al. (2018a) report a similar basin evolution due to syn-rift sedimentation. In their experiments without syn-rift sedimentation, the absence of sedimentary loading inside the graben leads to a smaller offset along the graben boundary faults since part of the deformation was taken up by intra-graben faults. By contrast, in their models with syn-rift sedimentation, the graben wedge was strengthened, so that faulting remained concentrated along the main graben boundary faults. The latter observation was also made in numerical models by Burov and Poliakov (2001) and Olive et al. (2014).

#### 4.1.2. Inversion phase

Our experimental results have established an order of importance regarding the parameters controlling fault reactivation throughout the inversion phase (Figs. 9b and 10b). It seems that the rift kinematics, i.e. orthogonal vs. oblique rifting, have no significant influence on inversion structures as the final rift structures were very similar. Much more important are syn-rift sedimentation and inversion kinematics.

Without sedimentation, the rift structures were reactivated during inversion, and new low-angle reverse faults developed independently of inversion direction (Fig. 9). Both orthogonal and oblique inversion resulted in the development of new low-angle reverse faults rooting at the base of the graben (Fig. 9). The reactivation of the rift structures occurred mainly at the intra graben structures in the orthogonal inversion models (Fig. 4 and 5; models B1 and B3), whereas in oblique inversion models (Fig. 4 and 5; models B2 and B4) both the graben boundary faults and the intra-graben faults showed significant reactivation.

The presence of syn-rift sediments (Fig. 10b) led to major differences in fault reactivation throughout the inversion phase, since the basin infill acted as a buffer to reactivation of the rift structures. Our models results are in accordance with previous studies that described a similar decrease in fault reactivation when syn-rift sedimentation was applied (Pinto et al., 2010a,b; del Ventisette et al., 2006; Panien et al., 2005b; Dubois et al., 2002). By contrast, Panien et al. (2005) found that graben infill increased rift fault reactivation. This difference was likely due to their use of rheologically weak microbeads as graben infill, while we used feldspar and quartz sands so that the graben infill in our models had a similar rheology to the surrounding granular materials.

Furthermore, we found that during orthogonal inversion graben faults did not undergo any reactivation as deformation localized in the newly formed low-angle reverse faults, whereas limited reactivation of previous rift structures was observed in our oblique inversion models (Fig. 10). Other studies, with different analogue modelling set-ups, have also shown that increasing degrees of oblique convergence can promote normal fault reactivation (e.g., Nalpas et al., 1995; Brun and Nalpas, 1996; see also reviews by Bonini et al. 2012 and Zwaan et al. 2022b), and references therein. Indeed, while analyzing inverted rift basins in nature, Ziegler et al. (1995) found that in order to facilitate normal fault reactivation the maximum horizontal compressive stress should be at an angle  $<45^\circ$  to the normal fault strike.

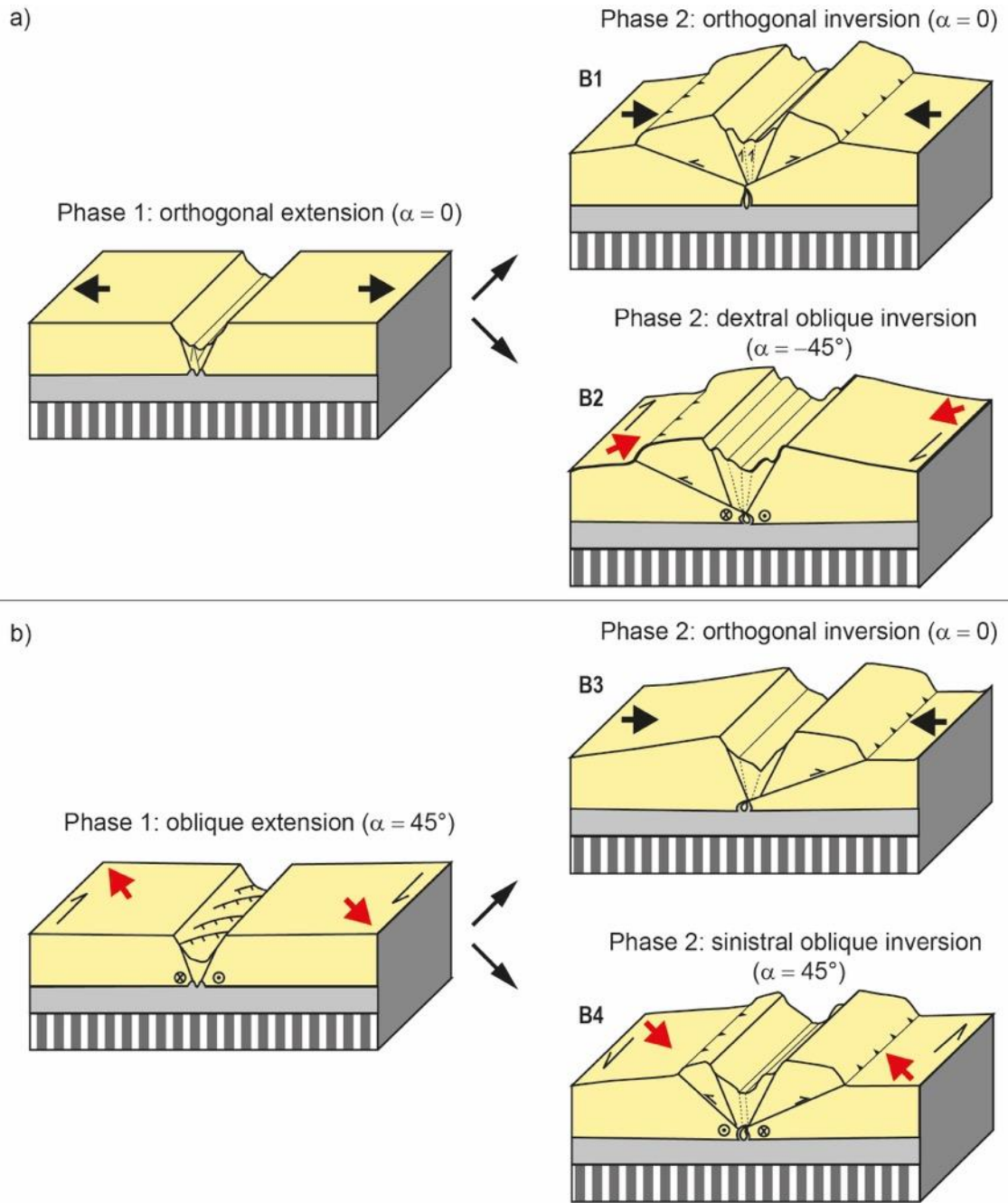


Figure 9: Schematic summary of our experimental results without syn-rift sedimentation



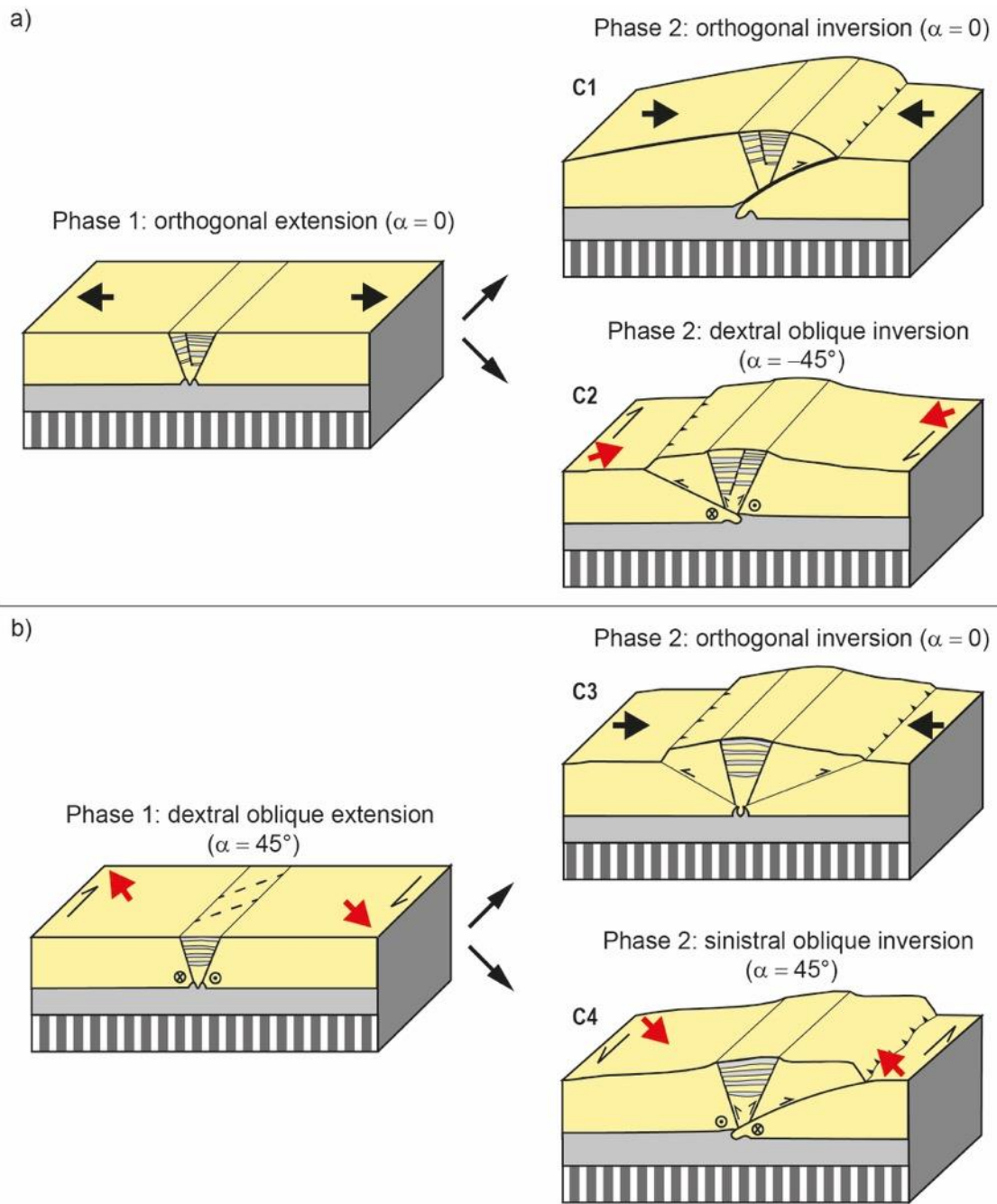


Figure 10: Schematic summary of our experimental results with syn-rift sedimentation

## 4.2 Comparing model results with the Araripe Basin

This study was inspired by the Late Jurassic/Early Cretaceous Araripe Basin in NE Brazil, which is presently situated at 1000 m above sea level (Assine, 2007). This elevation is due to post-rift inversion for which two end-member scenarios have been proposed (regional uplift or rift fault reactivation, Peulvast and Bétard, 2015, and Marques et al., 2014, respectively, Fig. 1). Here we revisit these scenarios in the context of our model results, and propose a third, updated scenario for inversion in the Araripe Basin.

The uplift of the Araripe Basin infill as explained by the Peulvast and Bétard (2015) scenario involves a large-scale rather than local basin inversion produced by regional uplift (Fig. 1). According to these authors, the present-day high standing mesa formation of the Araripe Basin is the result of differential erosion due to the presence of a strong sandstone formation covering the rift and post-rift sedimentary formations. However, other work demonstrates continuing [ENE–E–WSW](#) compression across the South American plate (Assumpção, 1992; Coblenz and Richardson, 1996; Lima, 2003; Marques et al., 2013; Assumpção et al., 2016), combined with fault inversion in the region (e.g. Bezerra et al., 2020; Vasconcelos et al., 2021), suggesting that compressional horizontal stresses must have played a role in the inversion of the Araripe Basin as well.

Marques et al. (2014) proposed that inversion of the basin resulted from such regional horizontal compression acting on the South American plate due to the opening of the South Atlantic Ocean to the east (ridge-push) and the development of the Andes Cordillera to the west. Furthermore, Marques et al. (2014) concluded that these combined stresses were the cause for reactivation and inversion of high angle normal faults. Additionally, the authors stated that the obliquity of the normal faults in relation to the inversion stresses, in combination with fluid injection along the fault planes, facilitated fault reactivation. However, although we observed some fault reactivation in our oblique inversion models, this reactivation did never lead to full inversion of the graben normal faults (Figs. 9 and 10). In fact, no large-scale normal fault reactivation has been observed on seismic sections from the Araripe Basin (Ponte and Ponte-filho, 1996). Instead, Rosa et al. (2023) described limited reverse movement and fault inversion during Early Cretaceous rifting, when the basin changed from a system undergoing NE-SW extension to a system undergoing NW-SE extension. These authors reported positive flower structures on seismic lines that only affected syn-rift units, and suggested that the inversion of normal faults, which Marques et al. (2014) attributed to the most recent inversion of the Araripe basin, might in fact have occurred locally during the initial rifting phase instead. Furthermore, the post-rift sediments of the Araripe Basin cover an area larger than the extent of the original rift grabens and were deposited directly over the pre-Cambrian basement (Assine, 2007), and large-scale offset of these post-rift units is not observed in the field.

However, recent work shows that mild post-rift fault inversion did take place in the basin (Cardoso, 2010) and also other studies detected inversion in basins from the same rifting system the Araripe Basin is part of (e.g. Rio do Peixe Basin, Potiguar Basin, Bezerra et al., 2020; Vasconcelos et al., 2021). These authors analysed seismic data and described a mild to moderate inversion along the normal faults of these basins, although no full-scale basin inversion *sensu* Marques et al. (2014) was observed. Similar observations are made on seismic sections from the Araripe Basin (Ponte and Ponte-filho, 1996), supporting the interpretation that horizontal shortening must have played a role in the inversion of the Araripe Basin.

However, this shortening must have been accommodated in some other way than large-scale normal fault inversion.

Our modelling results provide a solution to this apparent paradox, which involves the development of large-scale low-angle reverse faults during oblique convergence that take up most of the shortening, thus leading to basin uplift with some, but very limited, reactivation of the original rift structures (Fig. 11). Given the regional ENE-WSW shortening causing inversion of the Araripe Basin and the SW-NE-SW orientation of the initial grabens (Coblentz and Richardson, 1996; Marques et al., 2013; Fig. 1a), this oblique shortening was most likely of a dextral nature. Furthermore, our models suggest that initial rift kinematics did not have a strong impact on the later inversion structures, the right-stepping *en échelon* basin arrangement of the Araripe basin is similar to oblique rifting structures in our models (Figs. 1a, 5, 8-10), and may suggest an initial sinistral oblique rifting phase due to roughly E-W divergence, extension although this en echelon rift basin orientation may also be influenced by the NE-SW-oriented shear zones found in the basement (Fig. 1a; de Matos, 1992; Ponte and Ponte-Filho, 1996). Our new oblique inversion scenario also explains the relatively undeformed uplift of the post-rift sediments and is in line with observations from the nearby Rio de Peixe Basin. In this basin, which is situated to the NE of the Araripe Basin and is part of the same rift trend, Vasconcelos et al. (2021) described mild to moderate inversion along the rift faults, as well as reverse faulting in the basement outside the graben area. These observations of the Rio do Peixe Basin are in excellent agreement with our model results, and we propose that this same scenario ~~involving~~ can readily explain the ~~field observations from~~ structures observed in the Araripe Basin as well (Ponte and Ponte-filho, 1966; Cardoso, 2010, Rosa et al, 2023). In fact, Marques et al. (2014), who favoured large-scale reactivation of rift normal faults as the key inversion mechanism in the Araripe Basin, -also observed ~~reported the presence of some new reverse fault in the basement of the Araripe Basin area.~~ Furthermore, ~~t~~ The inferred presence of large low-angle reverse faults (with a strike-slip component) outside the original rift basin ~~as predicted by~~ in our models, combined with the observations from Marques et al. (2014) and other researchers discussed above, provides a strong incentive for further field investigations to verify our proposed scenario for inversion of the Araripe Basin.

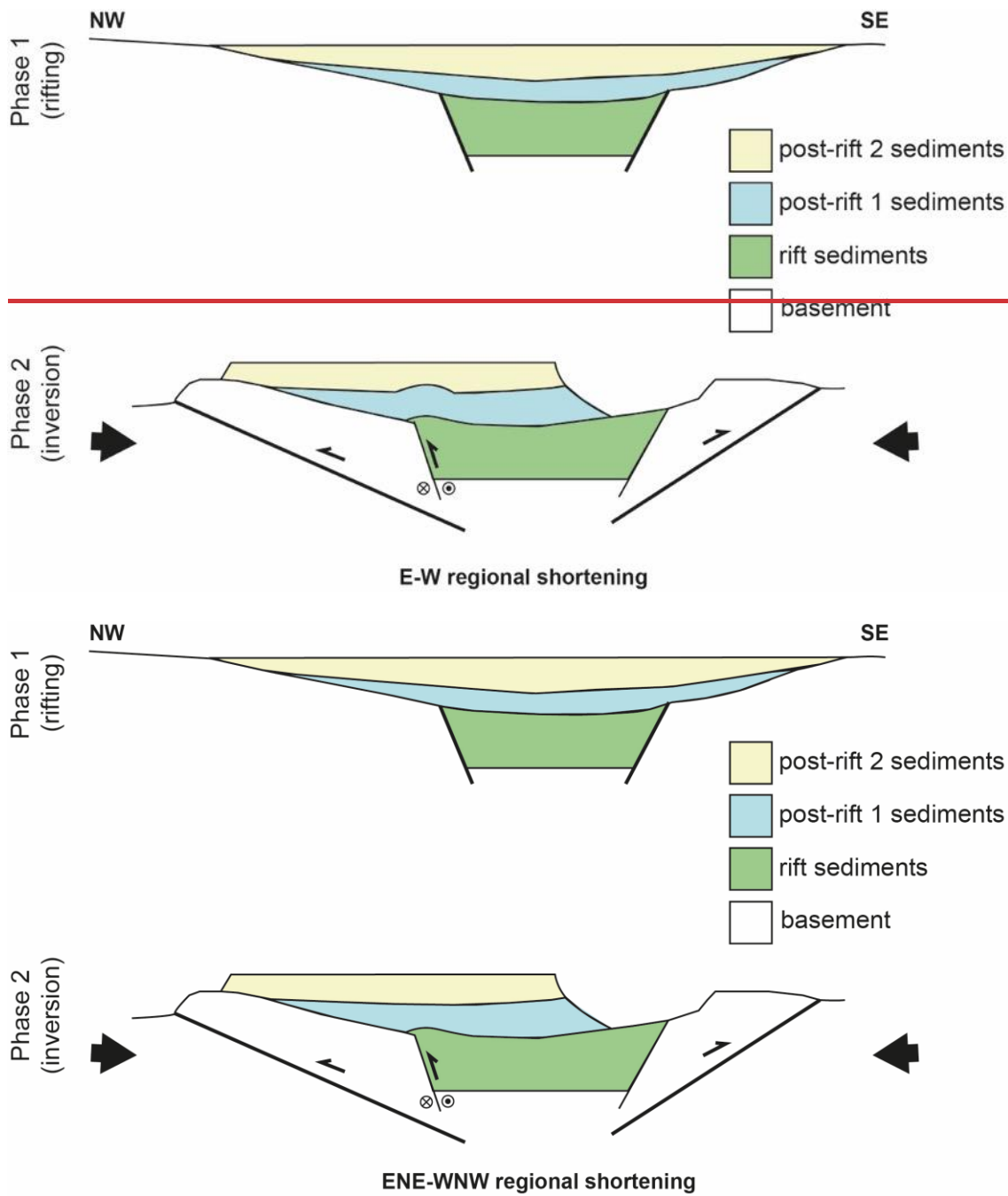


Figure 11: Proposed tectonic scenario for Araripe Basin inversion based on our analogue model results and data from literature. The scenario involves an initial rifting phase creating SW-NE oriented basins, followed by dextral oblique convergence due to general ENE-WSW oriented convergence. See text for details. Modified after Marques et al. (2014).

## 605 **5 Conclusions**

In this study we completed a series of new analogue modeling experiments aimed at evaluating the scenarios for basin inversion in the Araripe Basin in NE Brazil. We tested the influence of orthogonal or oblique extension, followed by either orthogonal or oblique convergence on rift development and on subsequent inversion structures. We find that:

610

- During rifting without sedimentation, orthogonal divergence creates through-going border faults, whereas oblique divergence leads to the initial formation of *en échelon* faults that eventually will link up to establish large graben boundary faults. Rift basins with syn-rift sedimentation follow a similar evolution, however the sedimentary loading increased subsidence compared to models without sedimentation.

615

- During inversion, a major part of the deformation is accommodated by newly formed low-angle reverse faults. Within that framework, models without sedimentation saw significant intra-graben fault reactivation, roughly independent of inversion direction (orthogonal or oblique). By contrast, in models with syn-rift sedimentation, inversion caused only minor reactivation of the original graben boundary faults during oblique convergence, due to the sedimentary infill acting as a buffer. Orthogonal convergence in models with syn-rift sediments did not lead to rift fault reactivation.

620

625

- An assessment of the existing scenarios for inversion of the Araripe basin with our model results as well as data from the field show that ~~these previous~~ scenarios do not fully explain all observations of the natural example. Therefore, based on our model results we propose an alternative scenario involving dextral oblique inversion and the development of low-angle reverse faults (with a strike-slip component) outside the basin. This scenario provides an incentive for future (field) studies.

630

### **Authors contributions**

635 PCR, FZ and GS planned and designed the experiments. PCR completed the experiments, analysed the model results, and wrote the first manuscript draft. FZ participated in running some of the experiments. FZ and TCS helped performing the model analysis. PCR, FZ, GS, RSS, TCS participated in the interpretation of the model results, and reviewed and edited the manuscript.

### **Competing interests**

640 The authors declare that they have no conflict of interest.

## Acknowledgements

645 PCR and RSS gratefully acknowledge the support from research and development project “Correlação  
estratigráfica, evolução paleoambiental e paleogeográfica e perspectivas exploratórias do Andar Alagoas”,  
sponsored by Shell Brasil Petróleo Ltda, and the strategic importance of the support given by ANP (Brazil's  
National Oil, Natural Gas and Biofuels Agency) through the R&D levy regulation (Technical Cooperation  
#20.219-2). PCR acknowledges CAPES – Coordination for the Improvement of Higher Education  
Personnel – for their financial support. FZ and TCS were funded by the Swiss National Science Foundation  
650 (via grant 200021-178731, <https://data.snf.ch/grants/grant/178731>, awarded to GS), which also covered the  
Open Access publication costs. FZ was also funded by a GFZ Discovery Fund fellowship. RSS  
acknowledges CNPq n° 311748/2018-0, FAPERJ n° E-26/200.995/2021 and Swiss National Science  
Foundation n° IZSEZ0\_191196/1 (<https://data.snf.ch/grants/grant/191196>) research grants. We thank  
Florian Ott and Kirsten Elger for helping us creating a GFZ data publication containing supplementary  
655 material (Richetti et al. in prep), reviewers Fernando Ornelas Marques and Ioan Munteanu for their  
constructive feedback, and editor Ernst Willingshofer for handling the review process.

## Data availability

Detailed overviews of model results are publicly available in the form of a GFZ data publication (Richetti  
et al. in prep).

660 Temporary link: [https://1drv.ms/u/s!AnD2tls1Utsrg\\_8b10PsZiOu7qn1Yw?e=KLkOdi](https://1drv.ms/u/s!AnD2tls1Utsrg_8b10PsZiOu7qn1Yw?e=KLkOdi)

Example of GFZ data publication: <https://doi.org/10.5880/fidgeo.2021.042>

## References

- Adam, J., Urai, J. L., Wieneke, B., Oncken, O., Pfeiffer, K., Kukowski, N., Lohrmann, J., Hoth, S., van der Zee, W., and Schmatz, J.: Shear localisation and strain distribution during tectonic faulting—new insights from granular-flow experiments and high-resolution optical image correlation techniques, *J Struct Geol*, 27, 283–301, <https://doi.org/10.1016/j.jsg.2004.08.008>, 2005.
- Assine, M. L.: Bacia do Araripe, *Boletim de Geociências da Petrobras*, 15, 371–389, 2007.
- Assumpcao, M.: The regional intraplate stress field in South America, *J Geophys Res*, 97, 11889, <https://doi.org/10.1029/91JB01590>, 1992.
- 665 Assumpção, M., Dias, F. L., Zevallos, I., and Naliboff, J. B.: Intraplate stress field in South America from earthquake focal mechanisms, *J South Am Earth Sci*, 71, 278–295, <https://doi.org/10.1016/j.jsames.2016.07.005>, 2016.
- Bezerra, F. H., de Castro, D. L., Maia, R. P., Sousa, M. O. L., Moura-Lima, E. N., Rossetti, D. F., Bertotti, G., Souza, Z. S., and Nogueira, F. C. C.: Postrift stress field inversion in the Potiguar Basin, Brazil – Implications for petroleum systems and evolution of the equatorial margin of South America, *Mar Pet Geol*, 111, 88–104, <https://doi.org/10.1016/J.MARPETGEO.2019.08.001>, 2020.
- 675 Bonini, M., Sani, F., and Antonielli, B.: Basin inversion and contractional reactivation of inherited normal faults: A review based on previous and new experimental models, *Tectonophysics*, 522–523, 55–88, <https://doi.org/10.1016/j.tecto.2011.11.014>, 2012.
- 680 Boutelier, D., Schrank, C., and Regenauer-Lieb, K.: 2-D finite displacements and strain from particle imaging velocimetry (PIV) analysis of tectonic analogue models with TecPIV, *Solid Earth*, 10, 1123–1139, <https://doi.org/10.5194/se-10-1123-2019>, 2019.
- Brito Neves, B. B., Santos, E. J., and van Schmus, W. R.: Tectonic history of the Borborema province, northeastern Brazil, in: 31st International Geological Congress, 151–182, 2000.
- 685 Broerse, T., Krstekanić, N., Kasbergen, C., and Willingshofer, E.: Mapping and classifying large deformation from digital imagery: application to analogue models of lithosphere deformation, *Geophys J Int*, 226, 984–1017, <https://doi.org/10.1093/gji/ggab120>, 2021.
- Brun, J.-P. and Nalpas, T.: Graben inversion in nature and experiments, *Tectonics*, 15, 677–687, <https://doi.org/10.1029/95TC03853>, 1996.
- 690 Buck, W. R.: Modes of continental lithospheric extension, *J Geophys Res Solid Earth*, 96, 20161–20178, <https://doi.org/10.1029/91JB01485>, 1991.
- Byerlee, J.: Friction of Rocks, in: *Rock Friction and Earthquake Prediction*, edited by: Byerlee, J. D. and Wyee, M., Birkhäuser Basel, Basel, 615–626, [https://doi.org/10.1007/978-3-0348-7182-2\\_4](https://doi.org/10.1007/978-3-0348-7182-2_4), 1978.
- 695 Camacho, C. R., Oliveira e Souza, F. R. F. R.: O arcabouço estrutural da Bacia Sedimentar do Araripe, Província Borborema, baseado em dados aeromagnetométricos, *Geol. USP, Série científica*, 17, 3, 149–161, <https://10.11606/issn.2316-9095.v17-393>, 20
- Cardoso, F. M. C.: O graben da Palestina: contribuição à estratigrafia e estrutura do estágio rifte na Bacia do Araripe, Nordeste do Brasil, Universidade Federal do Rio Grande do Norte, Natal, 1–129 pp., 2010.
- 700 Coblentz, D. D. and Richardson, R. M.: Analysis of the South American intraplate stress field, *J Geophys Res Solid Earth*, 101, 8643–8657, <https://doi.org/10.1029/96JB00090>, 1996.
- di Domenica, A., Petricca, P., Trippetta, F., Carminati, E., and Calamita, F.: Investigating fault reactivation during multiple tectonic inversions through mechanical and numerical modeling: An application to the Central-Northern Apennines of Italy, *J Struct Geol*, 67, 167–185, <https://doi.org/10.1016/j.jsg.2014.07.018>, 2014.

- 705 Dubois, A., Odonne, F., Massonnat, G., Lebourg, T., and Fabre, R.: Analogue modelling of fault reactivation: tectonic inversion and oblique remobilisation of grabens, *J Struct Geol*, 24, 1741–1752, [https://doi.org/10.1016/S0191-8141\(01\)00129-8](https://doi.org/10.1016/S0191-8141(01)00129-8), 2002.
- Ganade de Araujo, C. E., Weinberg, R. F., and Cordani, U. G.: Extruding the Borborema Province (NE-Brazil): A two-stage Neoproterozoic collision process, *Terra Nova*, 26, 157–168, <https://doi.org/10.1111/ter.12084>, 2014.
- 710 Guillaume, B., Gianni, G. M., Kermarrec, J.-J., and Bock, K.: Control of crustal strength, tectonic inheritance, and stretching/ shortening rates on crustal deformation and basin reactivation: insights from laboratory models, *Solid Earth*, 13, 1393–1414, <https://doi.org/10.5194/se-13-1393-2022>, 2022.
- Gurgel, S. P. P., Bezerra, F. H. R., Corrêa, A. C. B., Marques, F. O., and Maia, R. P.: Cenozoic uplift and erosion of structural landforms in NE Brazil, *Geomorphology*, 186, 68–84, <https://doi.org/10.1016/j.geomorph.2012.12.023>, 2013.
- 715 Hubbert, M. K.: Theory of scale models as applied to the study of geologic structures, *Geol Soc Am Bull*, 48, 1459–1520, <https://doi.org/10.1130/GSAB-48-1459>, 1937.
- Jara, P., Likerman, J., Charrier, R., Herrera, S., Pinto, L., Villarroel, M., and Winocur, D.: Closure type effects on the structural pattern of an inverted extensional basin of variable width: Results from analogue models, *J South Am Earth Sci*, 87, 157–173, <https://doi.org/10.1016/j.jsames.2017.10.018>, 2018.
- 720 Klinkmüller, M., Schreurs, G., Rosenau, M., and Kemnitz, H.: Properties of granular analogue model materials: A community wide survey, *Tectonophysics*, 684, 23–38, <https://doi.org/10.1016/j.tecto.2016.01.017>, 2016.
- 725 Lamarque, G. and Julià, J.: Lithospheric and sub-lithospheric deformation under the Borborema Province of NE Brazil from receiver function harmonic stripping, *Solid Earth Discussions*, 1–20, <https://doi.org/10.5194/se-2019-41>, 2019.
- Lima, C.: Ongoing compression across South American plate: observations, numerical modelling and some implications for petroleum geology, Geological Society, London, Special Publications, 209, 87–100, <https://doi.org/10.1144/GSL.SP.2003.209.01.09>, 2003.
- 730 Maestrelli, D., Montanari, D., Corti, G., del Ventisette, C., Moratti, G., and Bonini, M.: Exploring the Interactions Between Rift Propagation and Inherited Crustal Fabrics Through Experimental Modeling, *Tectonics*, 39, <https://doi.org/10.1029/2020TC006211>, 2020.
- Marques, F. O. and Nogueira, C. R.: Normal fault inversion by orthogonal compression: Sandbox experiments with weak faults, *J Struct Geol*, 30, 761–766, <https://doi.org/10.1016/j.jsg.2008.02.015>, 2008.
- 735 Marques, F. O., Nikolaeva, K., Assumpção, M., Gerya, T. V., Bezerra, F. H. R., do Nascimento, A. F., and Ferreira, J. M.: Testing the influence of far-field topographic forcing on subduction initiation at a passive margin, *Tectonophysics*, 608, 517–524, <https://doi.org/10.1016/j.tecto.2013.08.035>, 2013.
- 740 Marques, F. O., Nogueira, F. C. C., Bezerra, F. H. R., and de Castro, D. L.: The Araripe Basin in NE Brazil: An intracontinental graben inverted to a high-standing horst, *Tectonophysics*, 630, 251–264, <https://doi.org/10.1016/j.tecto.2014.05.029>, 2014.
- Marshak, S., Haq, S. S. B., and Sen, P.: Ramp initiation in fold-thrust belts: Insight from PIV analysis of sandbox models, *J Struct Geol*, 118, 308–323, <https://doi.org/10.1016/j.jsg.2018.11.006>, 2019.
- 745 de Matos, R. M. D.: The Northeast Brazilian Rift System, *Tectonics*, 11, 766–791, <https://doi.org/10.1029/91TC03092>, 1992.
- Molnar, N., Cruden, A., and Betts, P.: The role of inherited crustal and lithospheric architecture during the evolution of the Red Sea: Insights from three dimensional analogue experiments, *Earth Planet Sci Lett*, 544, 116377, <https://doi.org/10.1016/j.epsl.2020.116377>, 2020.



- 750 Molnar, N. E., Cruden, A. R., and Betts, P. G.: Interactions between propagating rifts and linear weaknesses in the lower crust, *Geosphere*, 15, 1617–1640, <https://doi.org/10.1130/GES02119.1>, 2019.
- Moulin, M., Aslanian, D., and Unternehr, P.: A new starting point for the South and Equatorial Atlantic Ocean, *Earth Sci Rev*, 98, 1–37, <https://doi.org/10.1016/j.earscirev.2009.08.001>, 2010.
- Mulugeta, G.: Squeeze box in a centrifuge, *Tectonophysics*, 148, 323–335, [https://doi.org/10.1016/0040-1951\(88\)90139-4](https://doi.org/10.1016/0040-1951(88)90139-4), 1988.
- 755 Nalpas, T., le Douaran, S., Brun, J. P., Unternehr, P., and Richert, J. P.: Inversion of the Broad Fourteens Basin (offshore Netherlands), a small-scale model investigation, *Sediment Geol*, 95, 237–250, [https://doi.org/10.1016/0037-0738\(94\)00113-9](https://doi.org/10.1016/0037-0738(94)00113-9), 1995.
- 760 Neto, F. L. S., Julià, J., and Schimmel, M.: Upper-mantle structure of the Borborema Province, NE Brazil, from P-wave tomography: Implications for rheology and volcanism, *Geophys J Int*, 216, 231–250, <https://doi.org/10.1093/gji/ggy421>, 2019.
- Nogueira, F. C. C., Marques, F. O., Bezerra, F. H. R., de Castro, D. L., and Fuck, R. A.: Cretaceous intracontinental rifting and post-rift inversion in NE Brazil: Insights from the Rio do Peixe Basin, *Tectonophysics*, 644–645, 92–107, <https://doi.org/10.1016/j.tecto.2014.12.016>, 2015.
- 765 Panien, M., Schreurs, G., and Pfiffner, A.: Sandbox experiments on basin inversion: Testing the influence of basin orientation and basin fill, *J Struct Geol*, 27, 433–445, <https://doi.org/10.1016/j.jsg.2004.11.001>, 2005.
- 770 Panien, M., Schreurs, G., and Pfiffner, A.: Mechanical behaviour of granular materials used in analogue modelling: insights from grain characterisation, ring-shear tests and analogue experiments, *J Struct Geol*, 28, 1710–1724, <https://doi.org/10.1016/j.jsg.2006.05.004>, 2006.
- Peulvast, J. P. and Bétard, F.: A history of basin inversion, scarp retreat and shallow denudation: The Araripe basin as a keystone for understanding long-term landscape evolution in NE Brazil, *Geomorphology*, 233, 20–40, <https://doi.org/10.1016/j.geomorph.2014.10.009>, 2015.
- 775 Pinto, L., Muñoz, C., Nalpas, T., and Charrier, R.: Role of sedimentation during basin inversion in analogue modelling, *J Struct Geol*, 32, 554–565, <https://doi.org/10.1016/J.JSG.2010.03.001>, 2010a.
- [Ponte, F. C., Ponte-Filho, F. C. \(1996\). Estrutura geológica e evolução tectônica da Bacia do Araripe. Recife: DNPM, Recife, p. 68.](#)
- Ramberg, H.: Gravity, Deformation and the Earth's Crust, Academic Press, London, 1981.
- 780 Ramos, G. V., Vasconcelos, D. L., Marques, F. O., de Castro, D. L., Nogueira, F. C. C., Bezerra, F. H. R., Perez, Y. A. R., Souza, J. A. B., and Medeiros, V. C.: Relations between inherited basement fabric and fault nucleation in a continental setting: The Rio do Peixe Basin, NE Brazil, *Mar Pet Geol*, 139, 105635, <https://doi.org/10.1016/j.marpetgeo.2022.105635>, 2022.
- 785 Rebelo, T. B., Batezelli, A., and Luna, J. S.: Stratigraphic evolution and carbonate factory implications: Case study of the Albian carbonates of the Campos Basin, Brazil, *The Depositional Record*, 7, 271–293, <https://doi.org/10.1002/dep2.118>, 2021.
- Richetti, P. C., Zwaan, F., Schreurs, G., Schmitt, R. S., Schmid, T. C.: Overviews and videos of top view imagery, topography data and DIC analysis results from analogue models of basin inversion. GFZ Data Services, in prep.
- 790 Rosa, M. C., Morales, N., and Assine, M. L.: Transtensional tectonics during the Gondwana breakup in northeastern Brazil: Early Cretaceous paleostress inversion in the Araripe Basin, *Tectonophysics*, 846, 229666, <https://doi.org/10.1016/j.tecto.2022.229666>, 2023.
- Schmid, T. C., Schreurs, G., and Adam, J.: Characteristics of continental rifting in rotational systems: New findings from spatiotemporal high resolution quantified crustal scale analogue models, *Tectonophysics*, 822, 229174, <https://doi.org/10.1016/J.TECTO.2021.229174>, 2022.

- 795 Schmid, T., Schreurs, G., Warsitzka, M., and Rosenau, M.: Effect of sieving height on density and friction of brittle analogue material: Ring-shear test data of quartz sand used for analogue experiments in the Tectonic Modelling Lab of the University of Bern, 2020.
- Schöfisch, T., Koyi, H., and Almqvist, B.: Magnetic Fabric Analyses of Basin Inversion: A Sandbox Modelling Approach, *EGU Sphere*, 1–20, <https://doi.org/10.5194/egusphere-2022-1258>, 2022.
- 800 Schreurs, G. and Colletta, B.: Analogue modelling of faulting in zones of continental transpression and transtension, *Geological Society, London, Special Publications*, 135, 59–79, <https://doi.org/10.1144/GSL.SP.1998.135.01.05>, 1998.
- Schreurs, G. and Colletta, B.: Analogue modelling of continental transpression, *Journal of the Virtual Explorer*, 07, <https://doi.org/10.3809/jvirtex.2002.00040>, 2002.
- 805 Sibson, R. H. and Scott, J.: Stress/fault controls on the containment and release of overpressured fluids: Examples from gold-quartz vein systems in Juneau, Alaska; Victoria, Australia and Otago, New Zealand, *Ore Geol Rev*, 13, 293–306, [https://doi.org/10.1016/S0169-1368\(97\)00023-1](https://doi.org/10.1016/S0169-1368(97)00023-1), 1998.
- Stanton, N., Ponte-Neto, C., Bijani, R., Masini, E., Fontes, S., and Flexor, J.-M.: A geophysical view of the Southeastern Brazilian margin at Santos Basin: Insights into rifting evolution, *J South Am Earth Sci*, 55, 141–154, <https://doi.org/10.1016/j.jsames.2014.07.003>, 2014.
- 810 Tron, V. and Brun, J.-P.: Experiments on oblique rifting in brittle-ductile systems, *Tectonophysics*, 188, 71–84, [https://doi.org/10.1016/0040-1951\(91\)90315-J](https://doi.org/10.1016/0040-1951(91)90315-J), 1991.
- Turner, J. P. and Williams, G. A.: Sedimentary basin inversion and intra-plate shortening, *Earth Sci Rev*, 65, 277–304, <https://doi.org/10.1016/J.EARSCIREV.2003.10.002>, 2004.
- 815 Vasconcelos, D. L., Marques, F. O., Nogueira, F. C. C., Perez, Y. A. R., Bezerra, F. H. R., Stohler, R. C., and Souza, J. A. B.: Tectonic inversion assessed by integration of geological and geophysical data: The intracontinental Rio do Peixe Basin, NE Brazil, *Basin Research*, 33, 705–728, <https://doi.org/10.1111/bre.12491>, 2021.
- Vauchez, A., Neves, S., Caby, R., Corsini, M., Egydio-Silva, M., Arthaud, M., and Amaro, V.: The Borborema shear zone system, NE Brazil, *J South Am Earth Sci*, 8, 247–266, [https://doi.org/10.1016/0895-9811\(95\)00012-5](https://doi.org/10.1016/0895-9811(95)00012-5), 1995.
- 820 del Ventisette, C., Montanari, D., Bonini, M., and Sani, F.: Positive fault inversion triggering “intrusive diapirism”: An analogue modelling perspective, *Terra Nova*, 17, 478–485, <https://doi.org/10.1111/j.1365-3121.2005.00637.x>, 2005.
- 825 del Ventisette, C., Montanari, D., Sani, F., and Bonini, M.: Basin inversion and fault reactivation in laboratory experiments, *J Struct Geol*, 28, 2067–2083, <https://doi.org/10.1016/J.JSG.2006.07.012>, 2006.
- Weijermars, R. and Schmeling, H.: Scaling of Newtonian and non-Newtonian fluid dynamics without inertia for quantitative modelling of rock flow due to gravity (including the concept of rheological similarity), *Physics of the Earth and Planetary Interiors*, 43, 316–330, [https://doi.org/10.1016/0031-9201\(86\)90021-X](https://doi.org/10.1016/0031-9201(86)90021-X), 1986.
- 830 Ziegler, P. A., Cloetingh, S., and van Wees, J.-D.: Dynamics of intra-plate compressional deformation: the Alpine foreland and other examples, *Tectonophysics*, 252, 7–59, [https://doi.org/10.1016/0040-1951\(95\)00102-6](https://doi.org/10.1016/0040-1951(95)00102-6), 1995.
- Zwaan, F. and Schreurs, G.: How oblique extension and structural inheritance influence rift segment interaction: Insights from 4D analog models, *Interpretation*, 5, SD119–SD138, <https://doi.org/10.1190/INT-2016-0063.1>, 2016.
- 835 Zwaan, F. and Schreurs, G.: How oblique extension and structural inheritance influence rift segment interaction: Insights from 4D analog models, *Interpretation*, 5, SD119–SD138, <https://doi.org/10.1190/INT-2016-0063.1>, 2017.

- 840 Zwaan, F., Chenin, P., Erratt, D., Manatschal, G., and Schreurs, G.: Competition between 3D structural inheritance and kinematics during rifting: Insights from analogue models, *Basin Research*, 34, 824–854, <https://doi.org/10.1111/bre.12642>, 2022a.
- Zwaan, F., Schreurs, G., Naliboff, J., and Buitter, S. J. H.: Insights into the effects of oblique extension on continental rift interaction from 3D analogue and numerical models, *Tectonophysics*, 693, 239–260, <https://doi.org/10.1016/j.tecto.2016.02.036>, 2016.
- 845 Zwaan, F., Schreurs, G., and Adam, J.: Effects of sedimentation on rift segment evolution and rift interaction in orthogonal and oblique extensional settings: Insights from analogue models analysed with 4D X-ray computed tomography and digital volume correlation techniques, *Glob Planet Change*, 171, 110–133, <https://doi.org/10.1016/j.gloplacha.2017.11.002>, 2018a.
- 850 Zwaan, F., Schreurs, G., Ritter, M., Santimano, T., and Rosenau, M.: Rheology of PDMS-corundum sand mixtures from the Tectonic Modelling Lab of the University of Bern (CH), *GFZ Data Services*, 1, 2018b.
- Zwaan, F., Schreurs, G., and Rosenau, M.: Rift propagation in rotational versus orthogonal extension: Insights from 4D analogue models, *J Struct Geol*, 135, 103946, <https://doi.org/10.1016/J.JSG.2019.103946>, 2020.
- 855 Zwaan, F., Schreurs, G., Buitter, S. J. H., Ferrer, O., Reitano, R., Rudolf, M., and Willingshofer, E.: Analogue modelling of basin inversion: a review and future perspectives, *Solid Earth*, 13, 1859–1905, <https://doi.org/10.5194/se-13-1859-2022>, 2022b.
- Zwaan, F., Schreurs, G., Rudolf, M., and Rosenau, M.: Ring-shear test data of feldspar sand FS900S used in the Tectonic Modelling Laboratory at the University of Bern (Switzerland), *GFZ Data Services*, <https://doi.org/10.5880/figeo.2022.008>, 2022c.
- 860